Received: 12 December 2017 | Revised: 23 July 2018 | Accepted: 9 August 2018

DOI: 10.1002/navi.272

ORIGINAL ARTICLE

WILEY ION

LTE receiver design and multipath analysis for navigation in urban environments

Kimia Shamaei | Zaher M. Kassas

Department of Electrical and Computer Engineering, University of California, Riverside, Riverside, California

Correspondence
Zaher M. Kassas, Department of Electrical and Computer Engineering, University of California, Riverside, 900 University Ave, Riverside, CA 92521.
Email: zkassas@ieee.org

Funding information
Office of Naval Research, Grant/Award Number: N00014-16-1-2305

Abstract

Mitigating multipath of cellular long-term evolution (LTE) signals for robust positioning in urban environments is considered. A computationally efficient receiver, which uses a phase-locked loop (PLL)–aided delay-locked loop (DLL) to track the received LTE signals, is presented. The PLL-aided DLL uses orthogonal frequency division multiplexing (OFDM)–based discriminator functions to estimate and track the time-of-arrival. The code phase and carrier phase performances in an additive white Gaussian noise (AWGN) channel are evaluated numerically. The effects of multipath on the code phase and carrier phase are analyzed, demonstrating robust multipath mitigation for high transmission LTE bandwidths. The average of the DLL discriminator functions over multiple LTE symbols is presented to reduce the pseudorange error. The proposed receiver is evaluated on a ground vehicle in an urban environment. Experimental results show a root mean square error (RMSE) of 3.17 m, a standard deviation of 1.06 m, and a maximum error of 6.58 m between the proposed LTE receiver and the GPS navigation solution over a 1.44 km trajectory. The accuracy of the obtained pseudoranges with the proposed receiver is compared against two algorithms: estimation of signal parameters by rotational invariance techniques (ESPRIT) and EKAT (ESPRIT and Kalman filter).

1 | INTRODUCTION

The inherently weak global navigation satellite system (GNSS) signals undergo severe attenuation in deep urban environments, making them unreliable for navigation.[1] Under these weak signal conditions, receivers cannot produce a navigation solution, since they cannot continuously track GNSS signals. Despite the inability to produce a navigation solution, some approaches use the received signal power, the periodicity of GPS satellites, and a power matching algorithm to estimate the receiver's state.[2,3] Other approaches use three-dimensional (3-D) building maps to predict satellite visibility via shadow matching to aid conventional range-based GNSS positioning.[4,5] The most common approach to address the limitations of GNSS-based navigation in urban environments is to fuse GNSS receivers with inertial navigation systems (INSs), lidars, cameras, and map matching algorithms.[6-8]

An alternative approach to these map-based and sensor-fusion–based approaches has emerged over the past decade. It exploits ambient signals of opportunity (SOPs), such as cellular, digital television, AM/FM, WiFi, and iridium satellite signals.[9-16] Among the different SOPs, cellular signals are particularly attractive due to their ubiquity, geometric diversity, high received power, and large bandwidth.[17] Cellular signals can be exploited for localization either to produce a navigation solution in a standalone fashion[18,19] or to aid the INS in the absence of GNSS signals.[20] Moreover, it has been demonstrated that fusing cellular signals with GNSS signals, when available, significantly improves the positioning accuracy.[21,22]

Multipath is arguably the most significant source of error when using cellular signals for positioning. Received cellular signals experience more multipath than GNSS signals, particularly for ground-based receivers in urban canyons, due to the low elevation angles at which signals are received.[23] High transmission bandwidth signals could resolve multipath, making cellular long-term evolution (LTE) signals attractive due to their large bandwidth.

The positioning performance achieved with LTE signals has been analyzed in the literature,[24-27] and several software-defined receivers (SDRs) have been proposed for navigation with real and laboratory-emulated LTE signals.[28-30] Experimental results demonstrated navigation solutions with different types of LTE reference signals in different environments, achieving meter-level accuracy.[17,23,30-32]

Five reference sequences in the received LTE signal have been studied for positioning: primary synchronization signal (PSS), secondary synchronization signal (SSS), cell-specific reference signal (CRS), positioning reference signal (PRS), and cyclic prefix (CP). Among these sequences, it was demonstrated that the CRS is always available and yields the most precise positioning due to its large transmission bandwidth.[23] CRS could have a bandwidth up to 20 MHz, which enables resolving the line-of-sight (LOS) signal from multipath signals in the environment. The CRS is transmitted to estimate the channel between the LTE base station (also known as Evolved Node B or eNodeB) and the user equipment (UE).

The CRS is scattered in the bandwidth and is transmitted in multiple symbols of the LTE frame, making the usage of computationally inexpensive delay-locked loops (DLLs) for tracking the signal infeasible. Several non-DLL–based approaches have been proposed. A super resolution algorithm (SRA)–based technique was developed in Driusso et al[33,34] to obtain the best case performance for positioning with CRS. While this method provided meter-level accuracy, it was computationally expensive and not suitable for real-time implementation. A first peak detection was proposed in del Peral-Rosado et al[28] and Shamaei et al[30] to obtain the time-of-arrival (TOA) using the CRS. While this method is computationally inexpensive, the first peak of the channel impulse response (CIR) cannot be detected when the multipath has a short range.

A novel, computationally efficient receiver that deals with the shortcomings of the SRA-based and first-peak-detection–based receivers was proposed in Shamaei et al.[35] In this receiver, a specialized orthogonal frequency division multiplexing (OFDM)–based DLL was designed to track the CRSs. This paper extends Shamaei et al.[35] and makes five contributions:

- A novel phase-locked loop (PLL) discriminator function is proposed to extract the carrier phase error from the CRS. The proposed PLL is used to aid the DLL, which reduces the TOA estimation error. The structure of the PLL and carrier phase discriminator function is discussed in detail.
- The average of the DLL discriminator functions over multiple LTE symbols is presented to reduce the pseudorange error, and the resulting error statistics are derived.
- The effects of multipath on the discriminator functions of the DLL and PLL are analyzed analytically and evaluated numerically.
- The performance of the proposed receiver is compared against two methods: estimation of signal parameters by rotational invariance techniques (ESPRIT)[36] and EKAT (ESPRIT and Kalman filter).[34] The comparison is made in terms of the accuracy of the produced pseudoranges and implementation cost.
- Experimental results are presented for a ground vehicle navigating in downtown Riverside, California, with the proposed LTE receiver. Despite navigating in a severe LTE multipath environment, it is demonstrated that the achieved root mean square error (RMSE) with four LTE eNodeBs was 3.17 m from a GPS navigation solution with 10 GPS satellites.

The proposed SDR has two main stages: acquisition and tracking. In the acquisition stage, the TOA initial estimate is first obtained by correlating the received signal with locally generated PSS and SSS. The PSS and SSS have less than 1 MHz transmission bandwidth, making them susceptible to multipath-induced error while estimating the TOA. Such error is then mitigated through the ESPRIT algorithm. In the ESPRIT algorithm, the CIR is estimated to differentiate the LOS from the multipath. In the tracking stage, the proposed PLL-aided DLL structure exploits the high transmission bandwidth of the CRS to further reduce multipath error. Therefore, the design approach of the proposed receiver is aimed at mitigating multipath for positioning with LTE signals in urban environments.

Throughout the paper, italic capital letters (eg, X) represent the frequency domain, italic small bold letters (eg, $\boldsymbol{x}$) represent vectors, and capital bold letters represent matrices (eg, $\mathbf{X}$). The letters i, k, n, and j represent the symbol, subcarrier, time index, and pseudorange measurement number, respectively. Note that each pseudorange measurement is obtained every one LTE frame. Therefore, j also shows the frame number.

The remainder of this paper is organized as follows. Section 2 presents a brief review of the LTE signal structure and received signal model. Section 3 discusses the receiver architecture. Section 4 analyzes the statistics of the code

and carrier phase errors. Section 5 discusses the navigation framework. Section 6 presents experimental results for a ground vehicle navigating exclusively with real LTE signals and compares the proposed receiver against the ESPRIT and EKAT algorithms. Section 7 concludes the paper and provides future work.

2 | LTE SIGNAL MODEL

In this section, the structure of the LTE signals is first discussed. Then, the signals that can be used for positioning in LTE systems are overviewed. Finally, the received signal model is presented.

2.1 | Frame structure

In LTE systems, the OFDM encoding scheme is used for data transmission. In OFDM, the transmitted symbols are mapped to different carrier frequencies called subcarriers, where a $\Delta f = 15$ kHz spacing is assigned between different subcarriers. Assuming that N_r subcarriers are allocated to data transmission, the transmitted serial data symbols must be first divided into groups of length N_r and mapped to each of these subcarriers. The mapping process depends on the LTE frame structure. Therefore, different data types are transmitted at different times and subcarriers. To reduce the interference on the received signal, a guard band is allocated to the OFDM signals, where no data are transmitted on the subcarriers at both sides of the N_r data subcarriers. This process is done by zero-padding the N_r data symbols to length N_c. Note that in LTE systems, no information is transmitted on direct current (DC) subcarrier. Next, an inverse fast Fourier transform (IFFT) is taken, resulting in an OFDM symbol in the time domain, which has a duration of $T_{symb} = 1/\Delta f$. The last L_{CP} elements of the symbol are repeated at the beginning to provide the CP and are used to suppress the interference due to multipath. Figure 1 summarizes the OFDM encoding scheme for a digital transmission.

In LTE systems, the values of N_r and N_c, which represent the bandwidth, are not unique and can be assigned to the values presented[37] in Table 1.

The resulting OFDM symbols are grouped into frames with a duration of $T_f = 10$ milliseconds. In frequency division duplexing (FDD) transmission, each frame is divided into 20 slots with a duration of 0.5 millisecond. Each slot with a normal CP allocation contains seven OFDM symbols. In a normal CP allocation, the CP of the first symbol of each slot has a duration of 5.21 μs and the rest of the symbols' CPs have a duration of 4.69 μs.

Since each data type is mapped to a specific time and symbol, the UE needs to exactly know the frame start time to be able to extract its data. To provide the frame start time to the UE, the PSS and SSS are transmitted in each frame. The UE can estimate the frame start time by finding the peak of the correlation of the received signal with the locally generated PSS and SSS. The structures of the PSS and SSS are discussed in details in the next subsection. Figure 2 shows an example of the LTE frame structure.

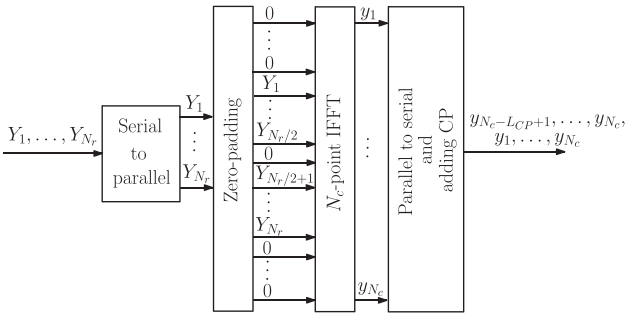

FIGURE 1 Block diagram of orthogonal frequency division multiplexing (OFMD) encoding scheme for a digital transmission. Abbreviation: CP, cyclic prefix; IFFT, inverse fast Fourier transform

TABLE 1 LTE system bandwidths and number of subcarriers

Bandwidth, MHz	Total Number of Subcarriers (N_c)	Number of Subcarriers Used (N_r)
1.4	128	72
3	256	180
5	512	300
10	1024	600
15	1536	900
20	2048	1200

Abbreviation: LTE, long-term evolution.

2.2 | Ranging signals

There are five different sequences in the received LTE signal that can be used for positioning: PSS, SSS, CP, PRS, and CRS. Note that these reference signals are broadcast in every LTE frame regardless of whether any data are transmitted to any UE. Therefore, it is always possible to use these reference signals for positioning. Besides, since the LTE reference signals are broadcast, the receiver does not need to be an authorized UE to be able to exploit these reference signals for navigation. This makes it possible to use the reference signals transmitted from eNodeBs of *different* network operators simultaneously.

The PSS and SSS are continual pilot signals transmitted to provide the frame start time to the UE. The PSS is a Zadoff-Chu sequence of length 62, which is transmitted on the last symbols of slots 0 and 10. The PSS is transmitted in one form of three possible sequences, each of which maps to an integer representing the sector ID of the eNodeB, ie, $N_{ID}^{(2)} \in \{0, 1, 2\}$.

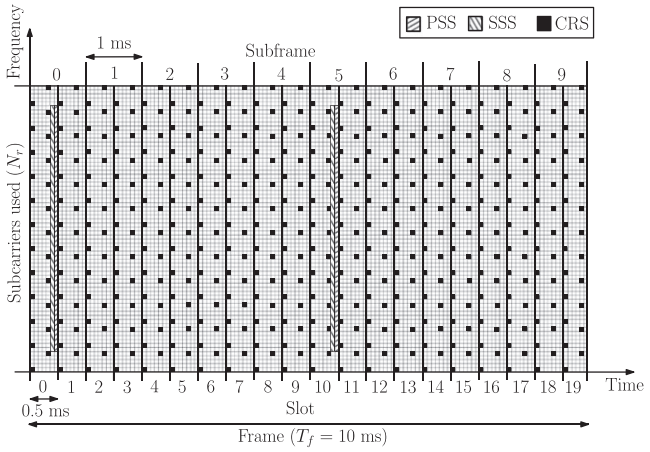

FIGURE 2 An example of the long-term evolution (LTE) frame structure with $N_r = 72$. Primary synchronization signal (PSS) and secondary synchronization signal (SSS) are transmitted on the middle 62 subcarriers. The last symbols of slots 0 and 10 are allocated to PSS. SSS is transmitted on the sixth symbol of slot 0 or 10. Cell-specific reference signal (CRS) is scattered in both frequency and time. CRS subcarriers are assigned based on the cell ID and symbol number

The SSS is also a sequence of length 62, which is transmitted on the sixth symbol of slot 0 or 10. This sequence is defined based on $N_{ID}^{(2)}$ and the slot number in which the SSS is transmitted such that different eNodeBs' SSS sequences are orthogonal to each other. The SSS is transmitted in one of 168 possible forms, each of which maps to an integer representing the eNodeB's group identifier, ie, $N_{ID}^{(1)} \in \{0, \cdots, 167\}$. By knowing $N_{ID}^{(1)}$ and $N_{ID}^{(2)}$, the UE can obtain the eNodeB's cell ID as[37,38]

$$N_{ID}^{Cell} = 3 \times N_{ID}^{(1)} + N_{ID}^{(2)}.$$

It has been shown analytically and experimentally that due to the low transmission bandwidth of the PSS and SSS, the estimated position using the PSS and SSS can have significantly high error in multipath environments.[27,39] Therefore, the PSS and SSS are more desirable for the acquisition stage.

An approach to estimate the time and frequency offset in an additive white Gaussian noise channel with CP was introduced in van de Beek et al.[40] However, the estimation results may have high error in multipath environments. Besides, since the transmitted CPs for different eNodeBs are not orthogonal, it is not possible to estimate TOAs for different eNodeBs using the CPs.

The PRS is a scattered pilot signal, which was introduced in LTE Release 9 for network-based positioning. In positioning with the PRS, the dedicated resources to the PRS are free from interference and the expected positioning accuracy is on the order of 50 m.[41] However, PRS-based positioning suffers from a number of drawbacks: (1) The user's privacy is compromised since the user's location is revealed to the network,[42] (2) localization services are limited only to paying subscribers and from a particular cellular provider, (3) ambient LTE signals transmitted by other cellular providers are not exploited, and (4) additional bandwidth is required to accommodate the PRS, which caused the majority of cellular providers to choose not to transmit the PRS in favor of dedicating more bandwidth for traffic channels. To circumvent these drawbacks, UE-based positioning approaches that exploit the CRS have been explored, where several advanced signal processing techniques were developed to achieve a performance similar to the PRS.[28,29,31,34,43]

The CRS is transmitted for channel estimation purposes and is scattered in time and bandwidth. The CRS sequence is defined based on the cell ID, allocated symbol, slot, and transmission antenna port number, such that different eNodeBs' CRS sequences are orthogonal to each other. The eNodeB's cell ID indicates the designated subcarriers to the CRS. In this paper, the CRS transmitted on the kth subcarrier and ith symbol is denoted by $S_i(k)$, where $k = m\Delta_{\text{CRS}} + \kappa, m = 0, \cdots, M-1, M = \lfloor N_r/\Delta_{\text{CRS}} \rfloor, \Delta_{\text{CRS}} = 6$, and κ is a constant shift depending on the cell ID and the symbol number i. In the sequel, for simplicity of notations, the subscript i is only used when it is required to indicate a specific symbol number. Figure 2 shows the PSS, SSS, and CRS.

2.3 | Received signal models

The OFDM symbol is transmitted in a multipath fading channel, which is assumed to stay constant over the duration of a symbol and has the CIR as

$$h(\tau) = \sum_{l=0}^{L-1} \alpha(l)\, \delta(\tau - \tau(l)),$$

where L is the number of multipath components; $\alpha(l)$ and $\tau(l)$ are the relative attenuation and delay components, respectively, of the lth path with respect to the first path; $\alpha(0) = 1$ and $\tau(0) = 0$; and δ is the Dirac delta function. Therefore, the received symbol after removing the CP and taking a fast Fourier transform (FFT) in a perfect synchronization condition will be

$$R(k) = \sqrt{C}\, Y(k) H(k) + W(k),$$
$$\text{for } k = 0, \cdots, N_c - 1,$$

where $Y(k)$ is transmitted OFDM symbol, C is the received signal power due to the antenna gain and any implementation loss, $W(k) \sim \mathcal{CN}(0, \sigma^2)$, where $\mathcal{CN}(a, b)$ denotes the complex Gaussian distribution with mean a and variance b, and

$$H(k) = \sum_{l=0}^{L-1} \alpha(l) e^{-j2\pi\tau(l)k/T_{symb}} \quad (1)$$

is the channel frequency response (CFR). In general, there is a mismatch between the estimated received symbol timing and the actual one, which can be due to imperfect synchronization, clock drift, Doppler frequency, and/or carrier frequency offset. Assuming that time mismatch is less than the CP duration, the received signal at the ith symbol can be rewritten as[44,45]

$$\begin{aligned} R_i(k) &= e^{j\pi e_f} e^{j2\pi(iN_t+L_{\text{CP}})e_f/N_c} e^{j2\pi e_\theta k/N_c} \sqrt{C} Y_i(k) H_i(k) \\ &\quad + W_i(k), \\ &\text{for } k = 0, \cdots, N_c - 1, \end{aligned} \quad (2)$$

where $N_t = N_c + L_{\text{CP}}$; $e_f = \frac{f_D}{\Delta f}$; f_D is the total carrier frequency offset due to the Doppler frequency, clock drift, and oscillators' mismatch; $e_\theta = \hat{\theta} - \theta$ is the symbol timing error normalized by the sampling interval $T_s = T_{symb}/N_c$; and $\hat{\theta}$ and θ are the normalized estimated and true symbol timings, respectively. Note that the first two exponentials in (2) model the effects of the carrier frequency offset and the third exponential models the effect of the symbol timing error. It is worth mentioning that Doppler frequency for each subcarrier is slightly different due to their different carrier frequencies. In this paper, this difference is neglected and the Doppler frequency is defined with respect to the center frequency f_c (in Hz).

3 | RECEIVER ARCHITECTURE

The structure of the proposed LTE SDR is shown in Figure 3. The proposed receiver has two main stages, namely, acquisition and tracking. In the following, the structure of each stage is discussed in detail.

3.1 | Acquisition

In the acquisition stage, nodes A, B, and C are first connected to node 1, where an initial estimate of the frame start time is obtained by acquiring the PSS and SSS. Then, nodes A, B, and C switch to node 2, in which the initial time estimate is refined using the ESPRIT algorithm and an initial estimate of the Doppler frequency is obtained. In this subsection, the acquisition stage is discussed in detail.

3.1.1 | Initial acquisition

In the first stage, nodes A, B, and C are connected to node 1. Here, the carrier is wiped off and the baseband samples of the OFDM symbols and their corresponding CPs are received at the UE as shown in Figure 4. The UE may start receiving a signal at any time of any frame. The UE needs to obtain the symbol start time to be able to remove the CPs and take the FFT to convert the signal to the frame structure. For this purpose, the UE first correlates the received signal with the locally generated time-domain PSS.[30] The PSS is transmitted twice per frame. Hence, the correlation result has two peaks in the duration of one frame, which is 10 milliseconds. Since the transmitted PSS sequences on slots 0 and 10 are the same, the UE cannot extract the symbol numbers from the correlation result and only the symbol start time can be obtained. Note that each type of signal is transmitted on a specific symbol and subcarrier of each frame. Therefore, knowing the symbol start time is

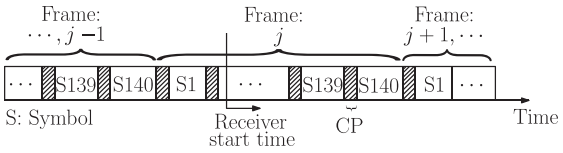

FIGURE 4 Received signal's samples structure. The receiver may start receiving the samples at any random time. Abbreviation: CP, cyclic prefix

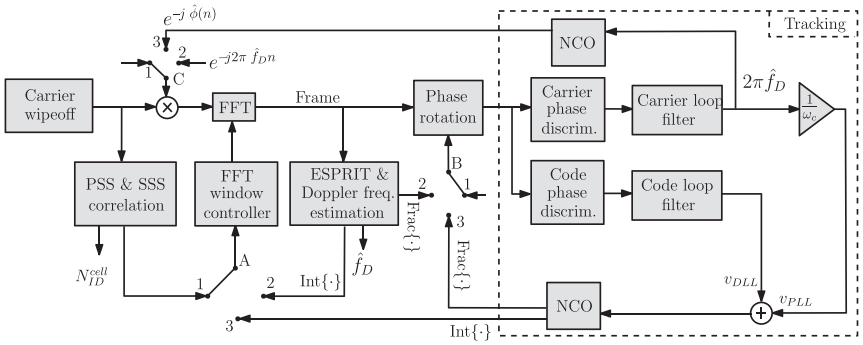

FIGURE 3 Block diagram of the proposed long-term evolution (LTE) receiver architecture. Abbreviation: ESPRIT, estimation of signal parameters by rotational invariance techniques; FFT, fast Fourier transform; NCO, numerically controlled oscillator; PSS, primary synchronization signal; SSS, secondary synchronization signal

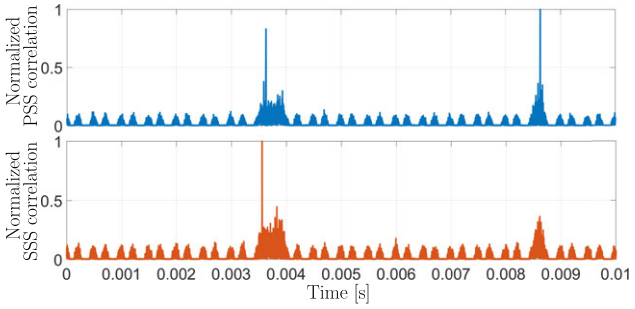

FIGURE 5 Primary synchronization signal (PSS) and secondary synchronization signal (SSS) normalized correlation results with real long-term evolution (LTE) signals [Color figure can be viewed at wileyonlinelibrary.com and www.ion.org]

not enough and the UE needs to exactly obtain the symbol numbers in each frame. Therefore, the signal is next correlated with the locally generated time-domain SSS. The SSS correlation result has only one peak, since the SSS is transmitted only once per frame. Since the SSS sequence depends on the slot number, it is possible to obtain the symbol number using the SSS correlation results. Figure 5 shows an example of the correlation of locally generated PSS and SSS with real LTE signals. The PSS and SSS have approximately 1 MHz bandwidth. The peak of the correlations may have a bias compared with the true frame timing in a multipath environment, which is modeled by symbol timing error presented in the received signal model in (2). In addition, due to the receiver's and transmitter's oscillator mismatches and Doppler frequency, a carrier frequency offset may remain in the received signal after carrier wipeoff. This is modeled by the total carrier frequency offset in (2).

3.1.2 | Acquisition refinement

In the second stage, nodes A, B, and C are connected to node 2. Here, the symbol timing error and carrier frequency offset are estimated and removed from the received signal. For this purpose, the CFR must first be estimated. In the symbols carrying the CRS, the transmitted signal $Y(k)$ is equal to the CRS sequence $S(k)$. Since the CRS sequence is known at the receiver, it is possible to estimate the CFR at the ith symbol as

$$\begin{aligned}\hat{H}_i(k) &= R_i(k)S_i^*(k),\\ &= \sqrt{C}\sum_{l=0}^{L-1}\alpha(l)e^{j\pi e_f}e^{j\frac{2\pi(iN_t+L_{\text{CP}})e_f}{N_c}}e^{j\frac{2\pi(e_\theta-\tau(l)/T_s)k}{N_c}}\\ &\quad + W'(k),\end{aligned} \tag{3}$$

for $k = m\Delta_{\text{CRS}} + \kappa, m = 0,\cdots,M-1$, and $W'(k) = W(k)S_i^*(k)$. The estimated CFR at the ith symbol and subcarriers allocated to the CRS can be rewritten as

$$\begin{aligned}\hat{H}'(m) &\triangleq \hat{H}_i(m\Delta_{\text{CRS}} + \kappa)\\ &= \sum_{l=0}^{L-1}\alpha'(l)e^{-j\frac{2\pi m\Delta_{\text{CRS}}\tau'(l)}{T_{symb}}} + W''(m)\\ &= \boldsymbol{a}^{\mathsf{T}}(m)\boldsymbol{\alpha} + W''(m),\\ &\text{for } m = 0,\cdots,M-1.\end{aligned} \tag{4}$$

where

$$\begin{aligned}\boldsymbol{\alpha} &= \left[\alpha'(0),\cdots,\alpha'(L-1)\right]^{\mathsf{T}},\\ \boldsymbol{a}(m) &= \left[e^{-j\frac{2\pi k\tau'(0)}{T_{symb}}},\cdots,e^{-j\frac{2\pi k\tau'(L-1)}{T_{symb}}}\right]^{\mathsf{T}},\\ \alpha'(l) &= \sqrt{C}e^{j\pi e_f}e^{j\frac{2\pi(iN_t+L_{\text{CP}})e_f}{N_c}}e^{-j\frac{2\pi\kappa\tau(l)}{T_{symb}}}\alpha(l),\\ \tau'(l) &= \tau(l) - T_s e_\theta,\\ W''(m) &= W'(m\Delta_{\text{CRS}} + \kappa).\end{aligned}$$

The set of estimated CFR over M different subcarriers can be written as

$$\begin{aligned}\hat{\boldsymbol{H}}' &= \left[\hat{H}'(0),\cdots,\hat{H}'(M-1)\right]^{\mathsf{T}}\\ &= \boldsymbol{A}\boldsymbol{\alpha} + \boldsymbol{W}'',\end{aligned}$$

where

$$\begin{aligned}\mathbf{A} &= [\boldsymbol{a}(0),\cdots,\boldsymbol{a}(M-1)]^{\mathsf{T}},\\ \boldsymbol{W}'' &= \left[W''(0),\cdots,W''(M-1)\right]^{\mathsf{T}}.\end{aligned}$$

The covariance matrix of the estimated channel $\hat{\boldsymbol{H}}'$ can be written as

$$\mathbf{R}_H = \mathbf{A}\mathbf{R}_\alpha\mathbf{A}^{\mathsf{H}} + \mathbf{R}_W,$$

where $\mathbf{R}_H, \mathbf{R}_\alpha$, and $\mathbf{R}_W$ are the covariance matrices of $\hat{\boldsymbol{H}}'$, $\boldsymbol{\alpha}$, and $\boldsymbol{W}''$, respectively, and H represents the Hermitian operator. It can be shown that $\mathbf{A}$ has L linearly independent vectors, which span the L-dimensional signal subspace. The goal is to find L independent vectors that best fit the observed CFR. Several methods have been proposed to solve this problem including multiple signal classification (MUSIC) and ESPRIT. The ESPRIT method has lower complexity compared with other approaches. It uses the rotational invariance properties of the subarrays of the subcarriers with respect to each other to estimate τ'.[36,46] To be able to use the ESPRIT algorithm, the channel length L must first be estimated. The minimum descriptive length (MDL) criterion is one approach to estimate L.[47] In this subsection, the MDL criterion and the ESPRIT algorithm are summarized. The details of the proof of each approach are provided in Roy and Kailath[36] and Wax and Kailath.[47]

Step 1: The data matrix $\mathbf{X}$ must first be constructed with snap shots of estimated CFR as

$$\mathbf{X} = \begin{bmatrix}\hat{H}'(0) & \hat{H}'(1) & \cdots & \hat{H}'(K-1)\\ \hat{H}'(1) & \hat{H}'(2) & \cdots & \hat{H}'(K)\\ \vdots & \vdots & \cdots & \vdots\\ \hat{H}'(P-1) & \hat{H}'(P) & \cdots & \hat{H}'(M-1)\end{bmatrix},$$

where P is the design parameter and $K = M - P + 1$.

Step 2: The channel length L can be estimated using the MDL metric. For this purpose, the singular value decomposition (SVD) of $\mathbf{X} = \mathbf{U}\Sigma\mathbf{V}^{\mathsf{H}}$ must be calculated, $\mathbf{U}$ and $\mathbf{V}$ are unitary matrices, and Σ is a rectangular diagonal matrix with singular values $\sigma_1 \geq \cdots \geq \sigma_P$ on the diagonal. Next, calculate the MDL criterion as

$$MDL(\gamma) = -K(P-\gamma)\log\left(\frac{\prod_{l=\gamma}^{P-1}\lambda_l^{1/(P-\gamma)}}{\frac{1}{P-\gamma}\sum_{l=\gamma}^{P-1}\lambda_l}\right) + \frac{1}{2}\gamma(2P-\gamma)\log K,$$
$$\text{for } \gamma = 0, \cdots, P-1,$$

where $\lambda_l = \sigma_l^2$. The estimate of L is obtained as

$$\hat{L} = \arg\min_{\gamma} MDL(\gamma).$$

Step 3: By knowing the channel length, it is possible to organize the eigenvectors corresponding to the $\hat{L}$ largest eigenvalues as $\mathbf{U}_s = \mathbf{U}\left[\mathbf{I}_{\hat{L}}\ \mathbf{0}_{\hat{L}\times(P-\hat{L})}\right]^{\mathsf{T}}$, where $\mathbf{I}_l$ is an identity matrix of size l and $\mathbf{0}_{l\times p}$ is an l-by-p matrix whose elements are zeros. Then, construct

$$\mathbf{U}_1 \triangleq \begin{bmatrix}\mathbf{I}_{P-1} & \mathbf{0}_{(P-1)\times 1}\end{bmatrix}\mathbf{U}_s,$$
$$\mathbf{U}_2 \triangleq \begin{bmatrix}\mathbf{0}_{(P-1)\times 1} & \mathbf{I}_{P-1}\end{bmatrix}\mathbf{U}_s.$$

Step 4: Finally, the ESPRIT rotational matrix must be constructed as

$$\Psi = \left(\mathbf{U}_1^{\mathsf{H}}\mathbf{U}_1\right)^{-1}\mathbf{U}_1^{\mathsf{H}}\mathbf{U}_2,$$

and compute its eigenvalues ψ_l, for $l = 0, \cdots, \hat{L} - 1$. The values of $\tau'(l)$ can be obtained as

$$\tau'(l) = -\frac{1}{2\pi T_s \Delta f \Delta_{\text{CRS}}}\arg\{\psi_l\}.$$

Since it was assumed that $\tau(0) = 0$ and $\tau'(l) = \tau(l) - T_s e_\theta$, the normalized estimated symbol timing error can be obtained as

$$\hat{e}_\theta = -\frac{1}{T_s}\min_l \tau'(l).$$

Note that in some environments, the direct signal may be blocked and the minimum of the estimated channel delays may not correspond to the LOS signal. However, differentiating the LOS signal from non-LOS (NLOS) signals is out of the scope of this paper.

The normalized estimated symbol timing error $\hat{e}_\theta$ can be divided into two parts: integer, $\text{Int}\{\cdot\}$, and fractional, $\text{Frac}\{\cdot\}$, given by

$$\hat{e}_\theta = \text{Int}\{\hat{e}_\theta\} + \text{Frac}\{\hat{e}_\theta\},$$

where $-1 \leq \text{Frac}\{\hat{e}_\theta\} \leq 0$.

Next, the initial Doppler frequency can be estimated, by measuring the difference between the received signals' phases on the same symbols of two consecutive slots. For this purpose, define $z(m)$ as

$$z(m) = R_{i+7}(k)R_i^*(k)S_{i+7}^*(k)S_i(k) = Ce^{j2\pi 7N_t e_f/N_c}|H_i(k)|^2 + W'(k), \quad \text{for } k = m\Delta_{\text{CRS}} + \kappa,\ m = 0, \cdots, M-1. \tag{5}$$

Then, the initial carrier frequency offset is estimated as

$$\hat{f}_D = \frac{1}{2\pi T_{slot}}\Delta\varphi, \tag{6}$$

where $T_{slot} = 0.5$ millisecond and

$$\Delta\varphi \triangleq \arg\left[\sum_{m=0}^{M-1} z(m)\right]. \tag{7}$$

Note that $\Delta\varphi$ is a function of the difference between the phases of two received signals at two different symbols. Since in this paper the sampling clock frequency offset is assumed to be negligible, $\Delta\varphi$ is defined according to (7). As such, the Doppler frequency estimate (6) ignores the sampling clock frequency offset. To include the effect of this offset, an approach such as the one described in Speth et al[48] could be adopted. The normalized estimated Doppler frequency is used to remove the initial phase estimate from the time-domain received signal as

$$r(n) \leftarrow e^{-j\hat{\phi}(n)}r(n),$$

where $r(n)$ is the time-domain received signal, $\hat{\phi}(n) = 2\pi\hat{f}_D n T_s$.

After removing the total carrier frequency offset estimate from the received signal $r(n)$, the integer part of the symbol timing error is used to control the FFT window. Then, the FFT is taken from $r(n)$ to convert the signal to the frequency domain $R(k)$. Next, the fractional part of the estimated symbol timing error is removed from $R(k)$ as

$$R'(k) \triangleq e^{-j2\pi k\text{Frac}\{\hat{e}_\theta\}/N_c}R(k).$$

Therefore, the ith received symbol on the subcarriers carrying the CRS after removing the symbol timing error estimate can be written as

$$R_i'(k) = e^{j\pi\tilde{e}_f}e^{j2\pi(iN_t+L_{\text{CP}})\tilde{e}_f/N_c}e^{j2\pi\tilde{e}_\theta k/N_c}\sqrt{C}S_i(k)H_i(k) + W_i(k), \quad \text{for } k = m\Delta_{\text{CRS}} + \kappa,\quad m = 0, \cdots, M-1, \tag{8}$$

where $\tilde{e}_f = e_f - \hat{e}_f$ is the remaining carrier frequency offset and $\tilde{e}_\theta = e_\theta - \hat{e}_\theta$ is the remaining symbol timing error.

3.2 | Tracking

In the tracking stage, nodes A, B, and C are connected to node 3, where a PLL-aided DLL is used to track the symbol timing. In this subsection, the structures of the PLL and DLL are discussed in detail.

3.2.1 | Phase-locked loop

A PLL has three main components: a carrier phase discriminator function, a carrier loop filter, and a numerically controlled oscillator (NCO). The carrier phase discriminator function is defined as

$$D_{\text{PLL}} = \arg\left[\sum_{m=0}^{M-1} R'(k)S^*(k)\right],$$
$$\text{for } k = m\Delta_{\text{CRS}} + \kappa, \quad m = 0, \cdots, M-1.$$

It can be shown that for $\tilde{e}_\theta \approx 0$, the PLL discriminator function for the ith received signal and in a multipath-free environment can be written as

$$D_{\text{PLL}} = \Delta\phi + N_{\text{PLL}} \quad ,$$

where $\Delta\phi = \pi\tilde{e}_f + 2\pi(iN_t + L_{\text{CP}})\tilde{e}_f/N_c$ and N_{PLL} is a zero-mean noise with variance

$$\text{var}\,[N_{\text{PLL}}] = \frac{\sigma^2}{2MC}\left(1 + \frac{\sigma^2}{2MC}\right). \tag{9}$$

A second-order PLL is used to track the carrier phase, with a loop filter transfer function given by

$$F_{\text{PLL}}(s) = 2\zeta\omega_{\text{PLL}} + \frac{\omega_{\text{PLL}}^2}{s}, \tag{10}$$

where ω_{PLL} is the undamped natural frequency of the phase loop and ζ is the damping ratio. The damping ratio was set to $1/\sqrt{2}$ to have a step response that rises fast enough with little overshoot.[49] Therefore, the PLL noise-equivalent bandwidth is $B_{\text{PLL}} = 0.53\omega_{\text{PLL}}$.[50] The output of the filter is the rate of change of the carrier phase error $2\pi\hat{f}_D$ expressed in rad/s. The phase loop filter transfer function in (10) is discretized and realized in state space. The loop update rate was set to a frame duration of T_f. An NCO is used to integrate the phase as

$$\phi(n) \leftarrow 2\pi\hat{f}_D n T_s + \phi(N_f),$$
$$\text{for } n = 0, \cdots, N_f,$$

where $N_f = T_f/T_s$ is the number of samples per frame. Then, the resulting phase is removed from the received signal as

$$r(n) \leftarrow e^{-j\phi(n)}r(n).$$

3.2.2 | Delay-locked loop

In conventional DLLs (eg, dot product), the TOA error is obtained as a function of the early, late, and prompt correlations, which are the correlation of the received signals with locally generated early (advanced), late (delayed), and prompt versions of the code sequence, respectively. The CRS is scattered in the bandwidth, which makes obtaining its time-equivalent form infeasible. As a result, obtaining the time-domain correlation of the received signal and the code will not be possible and conventional DLLs cannot be used to track the CRS. In this paper, a specialized DLL will be designed specifically for tracking the CRS in LTE systems.

A DLL has three main components: a code phase discriminator function, a code loop filter, and an NCO. Figure 6 shows the structure of the code phase discriminator function, which is an adaptation of Yang et al[45] for LTE systems.

Since a shift in the time domain is equivalent to a phase rotation in the frequency domain, the locally generated early and late code signals for the OFDM symbol can be obtained, respectively, as

$$S_{\text{early}}(m) = e^{-j2\pi m/M\xi}S(k),$$
$$S_{\text{late}}(m) = e^{j2\pi m/M\xi}S(k),$$
$$\text{for } k = m\Delta_{\text{CRS}} + \kappa, \quad m = 0, \cdots, M-1.$$

where $0 < \xi \leq 1/2$ is the normalized time shift. The early and late correlations in the frequency domain can be expressed, respectively, as

$$\mathcal{R}_{\text{early}} = \sum_{m=0}^{M-1} R'(m\Delta_{\text{CRS}} + \kappa)S^*_{\text{early}}(m),$$
$$\mathcal{R}_{\text{late}} = \sum_{m=0}^{M-1} R'(m\Delta_{\text{CRS}} + \kappa)S^*_{\text{late}}(m).$$

The discriminator function is defined as

$$D_{\text{DLL}} \triangleq |\mathcal{R}_{\text{early}}|^2 - |\mathcal{R}_{\text{late}}|^2 \triangleq M^2C\Lambda_{\text{DLL}}(\tilde{e}_\theta, \xi) + N_{\text{DLL}}, \tag{11}$$

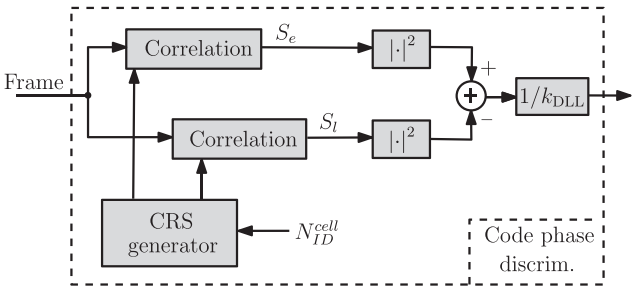

FIGURE 6 The structure of the code phase discriminator function. Abbreviation: CRS, cell-specific reference signal

where for a channel without multipath, $\Lambda_{\text{DLL}}(\tilde{e}_\theta, \xi)$ is the normalized S-curve function, defined as

$$\Lambda_{\text{DLL}}(\tilde{e}_\theta, \xi) \triangleq \left[\frac{\sin(\pi(\tilde{e}_\theta - \xi))}{M\sin(\pi(\tilde{e}_\theta - \xi)/M)}\right] - \left[\frac{\sin(\pi(\tilde{e}_\theta + \xi))}{M\sin(\pi(\tilde{e}_\theta + \xi)/M)}\right],$$

and N_{DLL} represents the noise with zero-mean and variance

$$\text{var}[N_{\text{DLL}}] \leq 2M^2\sigma^4\left[1 + \frac{C}{M\sigma^2}\left(\frac{\sin(\pi(\tilde{e}_\theta - \xi))}{\sin(\pi(\tilde{e}_\theta - \xi)/M)}\right)^2\right. \tag{12}$$

$$\left. + \frac{C}{M\sigma^2}\left(\frac{\sin(\pi(\tilde{e}_\theta + \xi))}{\sin(\pi(\tilde{e}_\theta + \xi)/M)}\right)^2\right], \tag{13}$$

where equality holds for $\xi = 0.5$.[45] In the following analysis, ξ is set to be 0.5. Figure 7 shows the normalized S-curve.

The output of the discriminator function is first normalized by the slope of the S-curve k_{DLL}, which represents the symbol timing error plus noise. Then, a DLL loop filter is used to achieve zero steady-state error. It can be assumed that the symbol timing error has linear variations, which can be due to the clock drift or receiver movement, and a second-order loop filter can provide zero steady-state error. Therefore, the normalized output of the discriminator function is first smoothed using a first-order low-pass filter (LPF) with a transfer function given by

$$F_{\text{DLL}}(s) = 2\zeta\,\omega_{\text{DLL}} + \frac{\omega_{\text{DLL}}^2}{s}, \tag{14}$$

where ω_{DLL} is the undamped natural frequency of the delay loop and ζ is the damping ratio. The damping ratio was set to $1/\sqrt{2}$ to have a step response that rises fast enough with little overshoot.[49] Therefore, the DLL noise-equivalent bandwidth is $B_{\text{DLL}} = 0.53\omega_{\text{DLL}}$.[50] The delay loop filter transfer function in (14) is discretized and realized in state space. The loop update rate was set to a frame duration of T_f.

Finally, the frame start time estimate is updated according to

$$\hat{e}_\theta \leftarrow \hat{e}_\theta - \frac{T_f}{T_s}(v_{DLL} + v_{PLL}),$$

where v_{DLL} is the output of the DLL filter, which is the rate of change of the symbol timing error expressed in s/s; $v_{PLL} = 2\pi\hat{f}_D/\omega_c$, where $\omega_c = 2\pi f_c$. The integer part of the frame start time estimate is used to control the FFT window, and the fractional part is removed using the phase rotation in R.

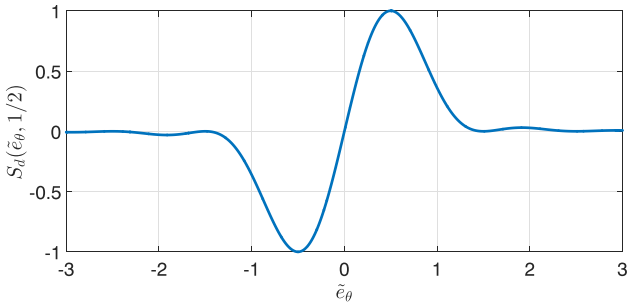

FIGURE 7 Discriminator function of the cell-specific reference signal (CRS) [Color figure can be viewed at wileyonlinelibrary.com and www.ion.org]

4 | STATISTICS OF THE CODE AND CARRIER PHASE ERRORS

In this section, the statistics of the code and carrier phase errors are derived for LTE signals.

4.1 | Code phase error in multipath-free environment

In a multipath-free and noise-free environment, the point at which the discriminator function is zero represents the TOA. However, noise can move the zero crossing point as

$$\tilde{e}_\theta = \frac{N_{\text{DLL}}}{k_{\text{DLL}}}, \tag{15}$$

where

$$k_{\text{DLL}} = \left.\frac{\partial D_{\text{DLL}}(\tilde{e}_\theta, \xi)}{\partial \tilde{e}_\theta}\right|_{\substack{\tilde{e}_\theta \approx 0 \\ \xi = 1/2}} = \frac{4\pi C\cos\left(\frac{\pi}{2M}\right)}{M\left(\sin\left(\frac{\pi}{2M}\right)\right)^3}. \tag{16}$$

Therefore, the open-loop code phase error due to noise is a random variable with zero-mean and variance

$$\sigma^2_{\tilde{e}_\theta} = \frac{\text{var}[N_{\text{DLL}}]}{k^2_{\text{DLL}}} \approx \frac{\pi^2}{128MC/N_0}, \tag{17}$$

which is obtained by assuming $M \gg 1$ and carrier-to-noise ratio $C/N_0 \gg 1$ dB-Hz and defining the power spectral density of noise as $S_n(f) \triangleq N_0/2 = \sigma^2$. Figure 8 plots the standard deviation of the pseudorange error as a function of C/N_0 for different values of N_c. The results show that the pseudorange error improves significantly as the number of subcarriers N_c in the LTE signal increases.

4.2 | DLL time integration

From (17), it can be seen that one of the parameters affecting the pseudorange error is the discriminator function's

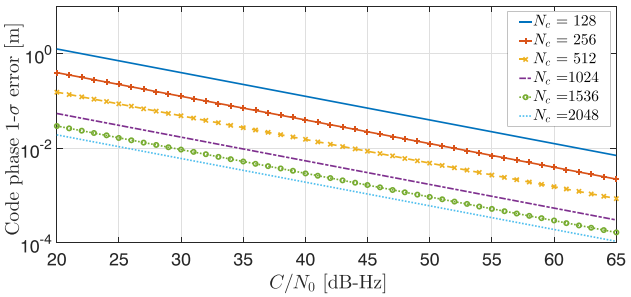

FIGURE 8 Standard deviation of the code phase error as a function of the C/N_0 for a different number of subcarriers N_c [Color figure can be viewed at wileyonlinelibrary.com and www.ion.org]

noise component. It can be shown that the average of I independent and identically distributed (i.i.d.) random variables reduces the variance by a factor of I. This property can be used to reduce the code phase error variance. By averaging the discriminator functions over I different symbols, the overall DLL discriminator function is obtained as

$$D_{\text{tot}} \triangleq \frac{1}{I}\sum_{i\in I_{CRS}} D_{\text{DLL}_i} = M^2 C\Lambda_{\text{DLL}}(\tilde{e}_\theta,\xi) + N_{\text{tot}}, \tag{18}$$

where I_{CRS} is the set of symbols over which integration is performed and contains CRS, $I = \text{card}\,(I_{CRS})$, where card$(\cdot)$ is the cardinality of the set, and

$$N_{\text{tot}} = \frac{1}{I}\sum_{i\in I_{CRS}} N_{\text{DLL}_i}.$$

It can be shown that $\{N_{\text{DLL}_i}\}_{i\in I_{CRS}}$ is i.i.d. with zero-mean and variance given in (12). Therefore, N_{tot} is zero-mean with variance $\text{var}[N_{\text{tot}}] = \text{var}[N_{\text{DLL}_i}]/I$. Using the discriminator function (18), it can be shown that the code phase error after averaging is a random variable with zero-mean and variance

$$\sigma^2_{\tilde{e}_\theta} \approx \frac{\pi^2}{128MIC/N_0}, \tag{19}$$

which is decreased by a factor of I compared with (17). Since the CRS is transmitted on multiple symbols in a frame, it is possible to take the average over the symbols carrying the CRS in only one frame while keeping the DLL loop update time equal to a frame duration. However, increasing I too much may result in loss of coherence due to unknown receiver motion and clock drift. Consequently, a very long integration time may degrade the estimation performance. The use of a dead-reckoning (DR)–type sensor may help compensate for receiver motion. On the other hand, the magnitude of the clock drift is determined solely by the oscillator stability. While stable oscillators (eg, oven-controlled crystal oscillators [OCXOs]) allow for longer integration time, they are expensive and large to install on cheap portable radio frequency (RF) platforms. An integration time of 400 milliseconds may be achieved for a stationary receiver using cheap, small, but less stable oscillators (eg, temperature-compensated crystal oscillators [TCXOs]).[51]

4.3 | Code phase error in a multipath environment

In a multipath fading environment, the discriminator function can be expressed as[45]

$$D_{\text{DLL}} = M^2 C\Lambda_{\text{DLL}}(\tilde{e}_\theta,\xi) + N_{\text{DLL}} + \chi_1 + \chi_2, \tag{20}$$

where χ_1 and χ_2 represent the multipath channel effect on the discriminator function according to

$$\begin{aligned}
\chi_1 = {} & C\left|\sum_{m=0}^{M-1}\sum_{l=1}^{L-1}\alpha(l)\,e^{-j2\pi(m/M)(\tau(l)/T_s+\tilde{e}_\theta-\xi)}\right|^2 \\
& - C\left|\sum_{m=0}^{M-1}\sum_{l=1}^{L-1}\alpha(l)\,e^{-j2\pi(m/M)(\tau(l)/T_s+\tilde{e}_\theta+\xi)}\right|^2, \\
\chi_2 = {} & 2C\Re\left\{\left[\sum_{m=0}^{M-1} e^{-j2\pi(m/M)(\tilde{e}_\theta-\xi)}\right]\right. \\
& \left.\cdot\left[\sum_{m'=0}^{M-1}\sum_{l=1}^{L-1}\alpha^*(l)e^{j2\pi(m'/M)(\tau(l)/T_s+\tilde{e}_\theta-\xi)}\right]\right\} \\
& - 2C\Re\left\{\left[\sum_{m=0}^{M-1} e^{-j2\pi(m/M)(\tilde{e}_\theta+\xi)}\right]\right. \\
& \left.\cdot\left[\sum_{m'=0}^{M-1}\sum_{l=1}^{L-1}\alpha^*(l)e^{j2\pi(m'/M)(\tau(l)/T_s+\tilde{e}_\theta+\xi)}\right]\right\},
\end{aligned}$$

where $\Re\{\cdot\}$ represents the real part. It can be seen from (20) that multipath adds a bias to the discriminator function. Figure 9 shows the code phase error in a multipath, but noise-free environment. The channel is assumed to have only two taps with $\alpha(0) = 1$ and $\alpha(1) = 0.2512e^{j\vartheta}$ (ie, the multipath amplitude is 6 dB lower than the LOS amplitude). The effect of the delay of the reflected signal, $\tau(1)$, on the pseudorange error is evaluated for $\vartheta = \{0,\pi\}$, ie, for constructive and destructive interferences, respectively. The results are obtained for different numbers of subcarriers. Figure 9 shows that the pseudorange error reduces in both constructive and destructive channels when the bandwidth of the LTE signal increases. With $N_c = 2048$, the pseudorange error with constructive multipath interference is less than 50 cm.

4.4 | Carrier phase error in multipath-free environment

In a noisy but multipath-free environment, noise can move the zero crossing point of the PLL discriminator function

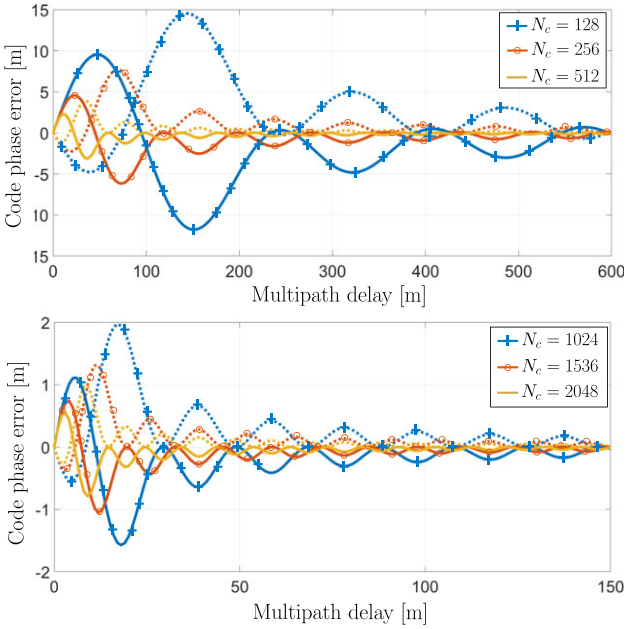

FIGURE 9 Code phase error for a multipath channel with $\alpha(0) = 1$ and $\alpha(1) = 0.2512$ and for different numbers of subcarriers. The solid and dashed lines represent constructive and destructive interferences, respectively [Color figure can be viewed at wileyonlinelibrary.com and www.ion.org]

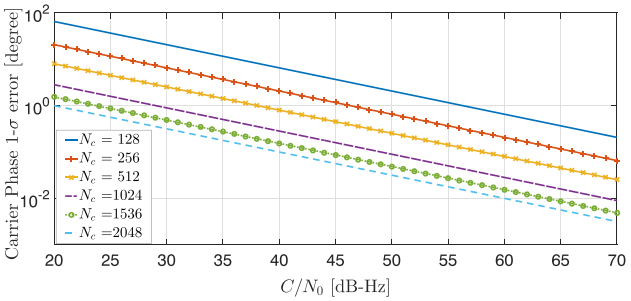

FIGURE 10 Standard deviation of the carrier phase error as a function of the C/N_0 for a different number of subcarriers N_c [Color figure can be viewed at wileyonlinelibrary.com and www.ion.org]

as

$$\Delta_\phi = \frac{N_{\text{PLL}}}{k_{\text{PLL}}}, \tag{21}$$

where $k_{\text{PLL}} = 1$. Therefore, the open-loop carrier phase error due to noise is a random variable with zero-mean and variance

$$\sigma^2_{\Delta\phi} = \frac{1}{4MC/N_0}\left(1 + \frac{1}{4MC/N_0}\right).$$

Figure 10 plots the standard deviation of the carrier phase error as a function of C/N_0 for different values of N_c. The results show that the carrier error improves significantly as the number of subcarriers N_c in the LTE signal increases.

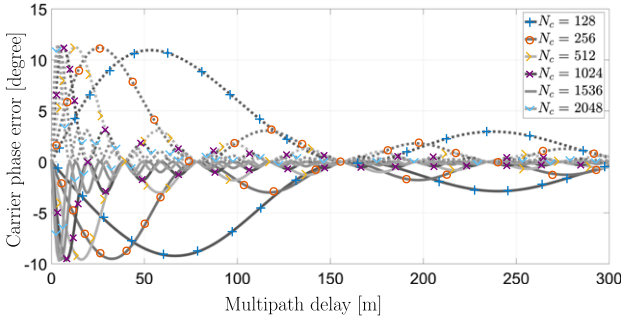

FIGURE 11 Carrier phase error for a multipath channel with $\alpha(0) = 1$ and $\alpha(1) = 0.2512$ and for a different number of subcarriers. The solid and dashed lines represent constructive and destructive interferences, respectively [Color figure can be viewed at wileyonlinelibrary.com and www.ion.org]

4.5 | Carrier phase error in a multipath environment

In a multipath fading environment, the PLL discriminator function can be expressed as

$$D_{\text{PLL}} = \arg\left[M\sqrt{C}e^{j\Delta\phi} + \chi_{\text{PLL}} + \text{noise}\right],$$
$$\text{for } k = m\Delta_{\text{CRS}} + \kappa, \quad m = 0, \cdots, M-1,$$

where

$$\chi_{\text{PLL}} = \sum_{m=0}^{M-1}\sum_{l=1}^{L-1}\sqrt{C}e^{j\Delta\phi}\alpha(l)e^{-j2\pi(m/M)(\tau(l)/T_s)}.$$

Figure 11 shows the carrier phase error in a multipath, but noise-free environment. The channel is assumed to be similar to Section 4.3. The results are obtained for a different number of subcarriers. Figure 9 shows that the maximum carrier phase error for a different number of subcarriers is the same. However, for higher N_c, the carrier phase error drops faster as the multipath delay increases.

5 | LTE NAVIGATION FRAMEWORK

The measured LTE pseudoranges by the proposed receiver are fed to an extended Kalman filter (EKF) to estimate the vehicle's state, given by

$$\boldsymbol{x}_r = \left[\boldsymbol{r}_r^{\mathsf{T}}, \dot{\boldsymbol{r}}_r^{\mathsf{T}}, c\delta t_r, c\dot{\delta} t_r\right]^{\mathsf{T}},$$

where $\boldsymbol{r}_r = [x_r, y_r, z_r]^{\mathsf{T}}$ is the receiver's 3-D position vector, δt_r is the receiver's clock bias, and $\dot{\delta} t_r$ is the receiver's clock drift. The state of the uth eNodeB is given by

$$\boldsymbol{x}_{s_u} = \left[\boldsymbol{r}_{s_u}^{\mathsf{T}}, c\delta t_{s_u}, c\dot{\delta} t_{s_u}\right]^{\mathsf{T}}, \quad u = 1, \cdots, N,$$

where $\boldsymbol{r}_{s_u} = \left[x_{s_u}, y_{s_u}, z_{s_u}\right]^{\mathsf{T}}$ is the uth eNodeB's 3-D position vector, δt_{s_u} is the eNodeB's clock bias, $\dot{\delta} t_{s_u}$ is the eNodeB's clock drift, and N is the total number of eNodeBs in the

environment. The pseudorange between the receiver and uth eNodeB at the jth time step can be expressed as

$$\rho_u(j) = \left\|\boldsymbol{r}_r(j) - \boldsymbol{r}_{s_u}\right\|_2 + c\cdot\left[\delta t_r(j) - \delta t_{s_u}(j)\right] + v_u(j), \quad \text{for } j = 1, 2, \cdots,$$

where v_u is the measurement noise, which is modeled as a zero-mean, white Gaussian random sequence with variance σ_u^2. The receiver's clock bias and drift are assumed to evolve according to the following discrete-time (DT) dynamics

$$\boldsymbol{x}_{\text{clk}_r}(j+1) = \mathbf{F}_{\text{clk}}\boldsymbol{x}_{\text{clk}_r}(j) + \boldsymbol{w}_{\text{clk}_r}(j), \tag{22}$$

where

$$\boldsymbol{x}_{\text{clk}_r} \triangleq \begin{bmatrix} c\delta t_r \\ c\dot{\delta} t_r \end{bmatrix}, \quad \mathbf{F}_{\text{clk}} = \begin{bmatrix} 1 & T \\ 0 & 1 \end{bmatrix}, \quad \boldsymbol{w}_{\text{clk}_r} = \begin{bmatrix} w_{\delta t_r} \\ w_{\dot{\delta} t_r} \end{bmatrix},$$

where $T \equiv T_f$ is the measurement's sampling time and $\boldsymbol{w}_{\text{clk}_r}$ is the process noise, which is modeled as a DT zero-mean white sequence with covariance $\mathbf{Q}_{\text{clk}_r}$ with

$$\mathbf{Q}_{\text{clk}_r} = \begin{bmatrix} S_{\tilde{w}_{\delta t_r}} T + S_{\tilde{w}_{\dot{\delta} t_r}} \frac{T^3}{3} & S_{\tilde{w}_{\dot{\delta} t_r}} \frac{T^2}{2} \\ S_{\tilde{w}_{\dot{\delta} t_r}} \frac{T^2}{2} & S_{\tilde{w}_{\dot{\delta} t_r}} T \end{bmatrix}.$$

The terms $S_{\tilde{w}_{\delta t_r}}$ and $S_{\tilde{w}_{\dot{\delta} t_r}}$ are the clock bias and drift process noise power spectra, respectively, which can be related to the power-law coefficients $\{h_\alpha\}_{\alpha=-2}^{2}$, which have been shown through laboratory experiments to characterize the power spectral density of the fractional frequency deviation $y(t)$ of an oscillator from nominal frequency according to $S_y(f) = \sum_{\alpha=-2}^{2} h_\alpha f^\alpha$. A common approximation involves only the h_0 and h_{-2} parameters, namely, $S_{\tilde{w}_{\delta t_r}} \approx \frac{h_{0_r}}{2}$ and $S_{\tilde{w}_{\dot{\delta} t_r}} \approx 2\pi^2 h_{-2_r}$.[52]

The uth eNodeBs' clock states $\boldsymbol{x}_{\text{clk}_{s_u}}$ evolve according to the same dynamic model as the receiver's clock state (22), except that the process noise is replaced with $\boldsymbol{w}_{\text{clk}_{s_u}} \triangleq \left[w_{\delta t_{s_u}}, w_{\dot{\delta} t_{s_u}}\right]^{\mathsf{T}}$, which is modeled as a DT zero-mean sequence with covariance $\mathbf{Q}_{\text{clk}_{s_u}}$.[53]

One of the main challenges in navigation with LTE signals is the unavailability of the eNodeBs' positions and clock states. It has been previously shown that the SOP position can be mapped with a high degree of accuracy, whether collaboratively or noncollaboratively.[53,54] In what follows, the eNodeBs' positions are assumed to be known, and an EKF will be utilized to estimate the vehicle's position $\boldsymbol{r}_r$ and velocity $\dot{\boldsymbol{r}}_r$ simultaneously with the difference between the receiver and each eNodeB's clock bias and drift states. The difference between the receiver's clock state vector and the uth eNodeB's clock state vector $\Delta\boldsymbol{x}_{\text{clk}_u} \triangleq \boldsymbol{x}_{\text{clk}_r} - \boldsymbol{x}_{\text{clk}_{s_u}}$ evolves according to

$$\Delta\boldsymbol{x}_{\text{clk}_u}(j+1) = \mathbf{F}_{\text{clk}}\Delta\boldsymbol{x}_{\text{clk}_u}(j) + \boldsymbol{w}_{\text{clk}_u}(j),$$

where $\boldsymbol{w}_{\text{clk}_u} \triangleq \left(\boldsymbol{w}_{\text{clk}_r} - \boldsymbol{w}_{\text{clk}_{s_u}}\right)$ is a DT zero-mean white sequence with covariance $\mathbf{Q}_{\text{clk}_u}$, where $\mathbf{Q}_{\text{clk}_u} \triangleq \mathbf{Q}_{\text{clk}_r} + \mathbf{Q}_{\text{clk}_{s_u}}$.

The receiver is assumed to move in a two-dimensional (2-D) plane with known height, ie, $z(j) = z_0$ and $\dot{z}(j) = 0$, where z_0 is a known constant. Moreover, the receiver's 2-D position is assumed to evolve according to a velocity random walk, with the continuous-time (CT) dynamics given by

$$\ddot{x}_r(t) = \tilde{w}_x, \quad \ddot{y}_r(t) = \tilde{w}_y, \tag{23}$$

where $\tilde{w}_x$ and $\tilde{w}_y$ are zero-mean white noise processes with power spectral densities $\tilde{q}_x$ and $\tilde{q}_y$, respectively. The receiver's DT dynamics are hence given by

$$\boldsymbol{x}_{\text{pv}}(j+1) = \mathbf{F}_{\text{pv}}\boldsymbol{x}_{\text{pv}}(j) + \boldsymbol{w}_{\text{pv}}(j),$$

where

$$\boldsymbol{x}_{\text{pv}} \triangleq \begin{bmatrix} x_r \\ y_r \\ \dot{x}_r \\ \dot{y}_r \end{bmatrix}, \quad \mathbf{F}_{\text{pv}} = \begin{bmatrix} 1 & 0 & T & 0 \\ 0 & 1 & 0 & T \\ 0 & 0 & 1 & 0 \\ 0 & 0 & 0 & 1 \end{bmatrix},$$

and $\boldsymbol{w}_{\text{pv}}$ is a DT zero-mean white sequence with covariance $\mathbf{Q}_{\text{pv}}$, where

$$\mathbf{Q}_{\text{pv}} = \begin{bmatrix} \tilde{q}_x\frac{T^3}{3} & 0 & \tilde{q}_x\frac{T^2}{2} & 0 \\ 0 & \tilde{q}_y\frac{T^3}{3} & 0 & \tilde{q}_y\frac{T^2}{2} \\ \tilde{q}_x\frac{T^2}{2} & 0 & \tilde{q}_x T & 0 \\ 0 & \tilde{q}_y\frac{T^2}{2} & 0 & \tilde{q}_y T \end{bmatrix}.$$

The augmented state vector which will be estimated by the EKF is defined as $\boldsymbol{x} \triangleq \left[\boldsymbol{x}_{\text{pv}}^{\mathsf{T}}, \Delta\boldsymbol{x}_{\text{clk}_1}^{\mathsf{T}}, \cdots, \Delta\boldsymbol{x}_{\text{clk}_N}^{\mathsf{T}}\right]^{\mathsf{T}}$. This vector has the dynamics

$$\boldsymbol{x}(j+1) = \mathbf{F}\boldsymbol{x}(j) + \boldsymbol{w}(j),$$

where $\mathbf{F} \triangleq \text{diag}\left[\mathbf{F}_{\text{pv}}, \mathbf{F}_{\text{clk}}, \cdots, \mathbf{F}_{\text{clk}}\right]$ and $\boldsymbol{w}$ is a DT zero-mean white sequence with covariance $\mathbf{Q} \triangleq \text{diag}\left[\mathbf{Q}_{\text{pv}}, \mathbf{Q}_{\text{clk}}\right]$ and

$$\mathbf{Q}_{\text{clk}} = \begin{bmatrix} \mathbf{Q}_{\text{clk}_r} + \mathbf{Q}_{\text{clk}_{s_1}} & \mathbf{Q}_{\text{clk}_r} & \cdots & \mathbf{Q}_{\text{clk}_r} \\ \mathbf{Q}_{\text{clk}_r} & \mathbf{Q}_{\text{clk}_r} + \mathbf{Q}_{\text{clk}_{s_2}} & \cdots & \mathbf{Q}_{\text{clk}_r} \\ \vdots & \vdots & \ddots & \vdots \\ \mathbf{Q}_{\text{clk}_r} & \mathbf{Q}_{\text{clk}_r} & \cdots & \mathbf{Q}_{\text{clk}_r} + \mathbf{Q}_{\text{clk}_{s_N}} \end{bmatrix}.$$

Note that the proposed estimator assumed the receiver to be mobile. For the stationary receiver case, a more advanced estimator (eg, multiple model [MM]–type estimator[52]) could be employed. In this case, one mode of the estimator could be matched to velocity random walk dynamics, while the other mode could be matched

to stationary dynamics. In practice, the receiver is typically coupled with an inertial measurement unit (IMU), which is used to propagate the estimator's state between measurement updates from eNodeBs.[20]

6 | EXPERIMENTAL RESULTS

To evaluate the performance of the proposed receiver, an experiment was conducted using a ground vehicle in an urban multipath environment: downtown Riverside, California. In this section, the experimental setup and results are discussed.

6.1 | Experimental setup

In this experiment, a ground vehicle was equipped with two consumer-grade 800/1900 MHz cellular omnidirectional Laird antennas to receive the LTE signals at 739 and 1955 MHz carrier frequencies. These frequencies are used by the US LTE provider AT&T. A dual-channel National Instruments (NI) universal software radio peripheral (USRP)-2954R, driven by a GPS-disciplined oscillator (GPSDO) was used to simultaneously down-mix and synchronously sample LTE signals with 20 Msps. The vehicle was also equipped with one surveyor-grade Leica antenna to receive GPS signals. The GPS signal, which was down-mixed and sampled by a single-channel NI USRP-2930, was used to discipline the USRP clock oscillators, and samples of the GPS signal were stored and later used to produce the vehicle's "ground truth" trajectory. A laptop was used to store the GPS and LTE signals for postprocessing. Figure 12 shows the experimental setup.

It is assumed that the receiver had access to GPS, and GPS was cut off at the start time of the experiment. Therefore, the EKF's states were initialized with the values obtained from the GPS navigation solution. The standard deviation of the initial uncertainty of position and velocity were set to be 5 m and 0.01 m/s, respectively.[49] The standard deviation of the initial uncertainty of the clock bias and drift were set to be 0.1 m and 0.01 m/s, respectively, which were obtained empirically.

According to the LTE protocol, the modulated carrier frequency of LTE signals received from an eNodeB over 1 millisecond should be accurate to within ±50 parts per billion (ppb) with respect to a reference.[55] This reference is typically obtained by using OCXOs in the eNodeBs and the signals transmitted by GNSS. However, when GNSS signals are not available or reliable (eg, in deep urban canyons), other standards (eg, synchronous ethernet) could be used to transfer synchronization signals to the eNodeBs.[55,56]

TABLE 2 ENodeBs' characteristics

eNodeB	Carrier Frequency, MHz	N_{ID}^{Cell}	Bandwidth, MHz
1	739	152	10
2	1955	216	20
3	739	232	10
4	739	288	10

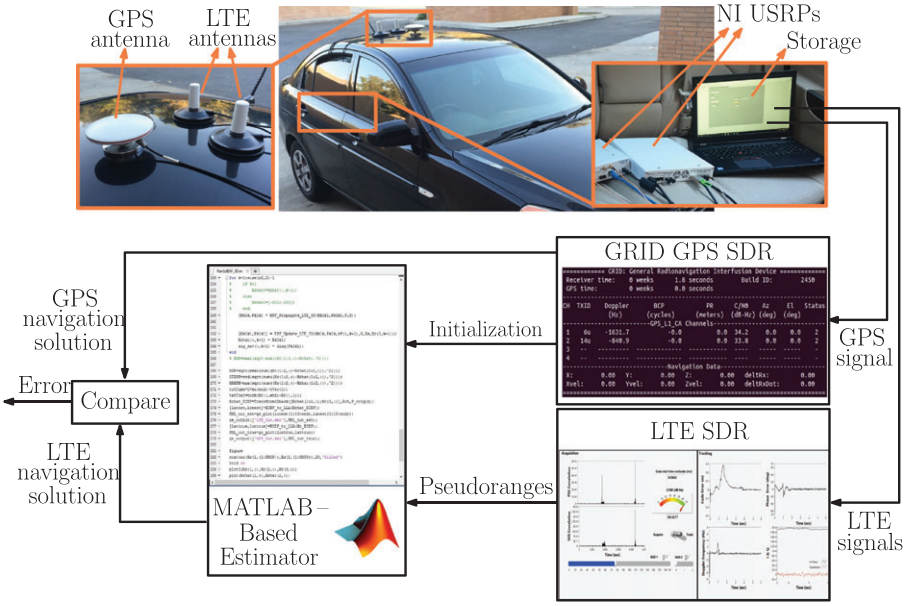

FIGURE 12 Experimental hardware and software setup. Abbreviations: GRID, generalized radionavigation interfusion; LTE, long-term evolution; NI, National Instruments; SDR, software-defined receiver; USPR, universal software radio peripheral [Color figure can be viewed at wileyonlinelibrary.com and www.ion.org]

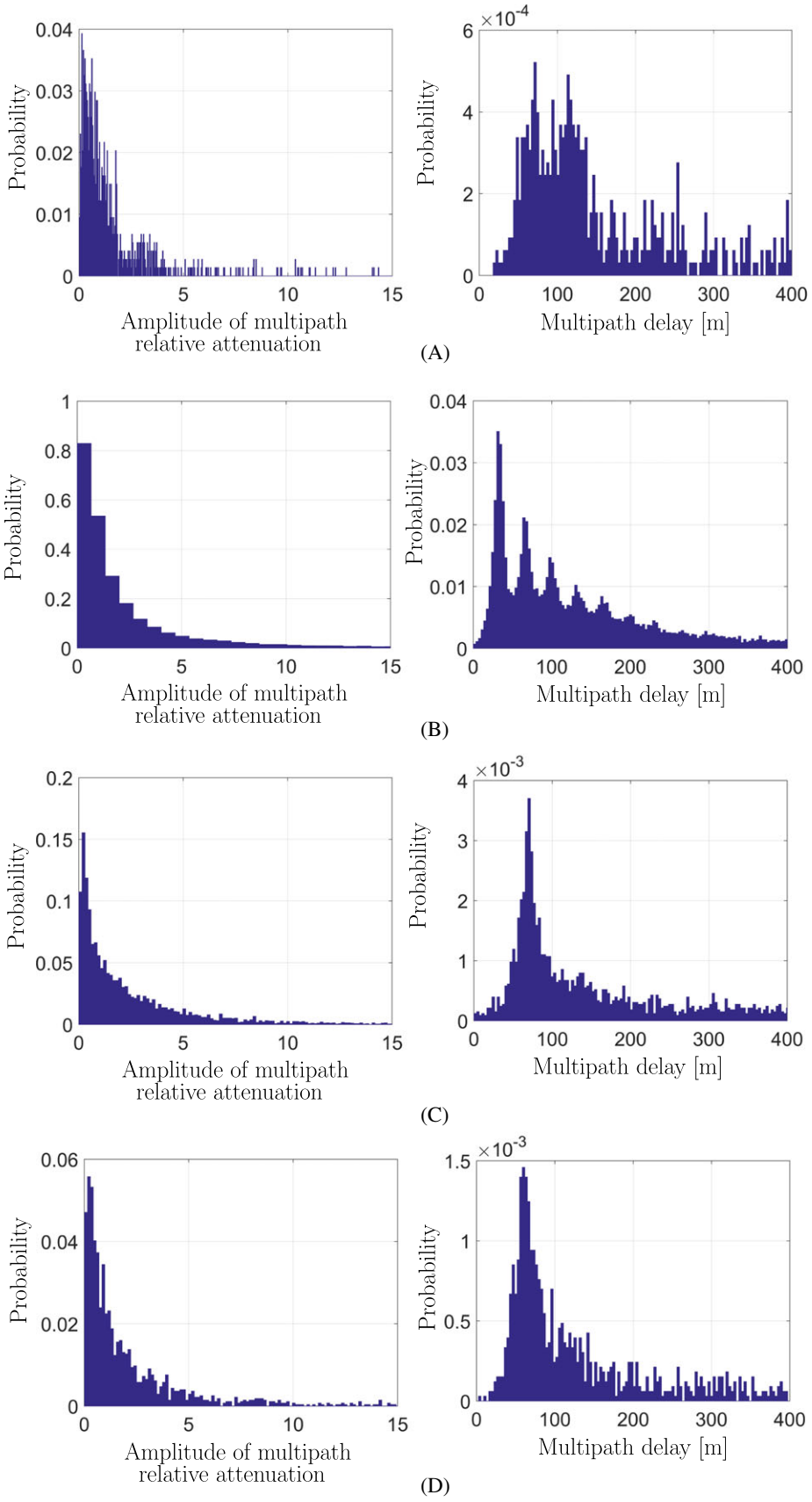

FIGURE 13 A-D, The probability of the relative (with respect to the first estimated path) attenuation and delay components of the multipath over the course of experiment, for eNodeBs 1 through 4, respectively [Color figure can be viewed at wileyonlinelibrary.com and www.ion.org]

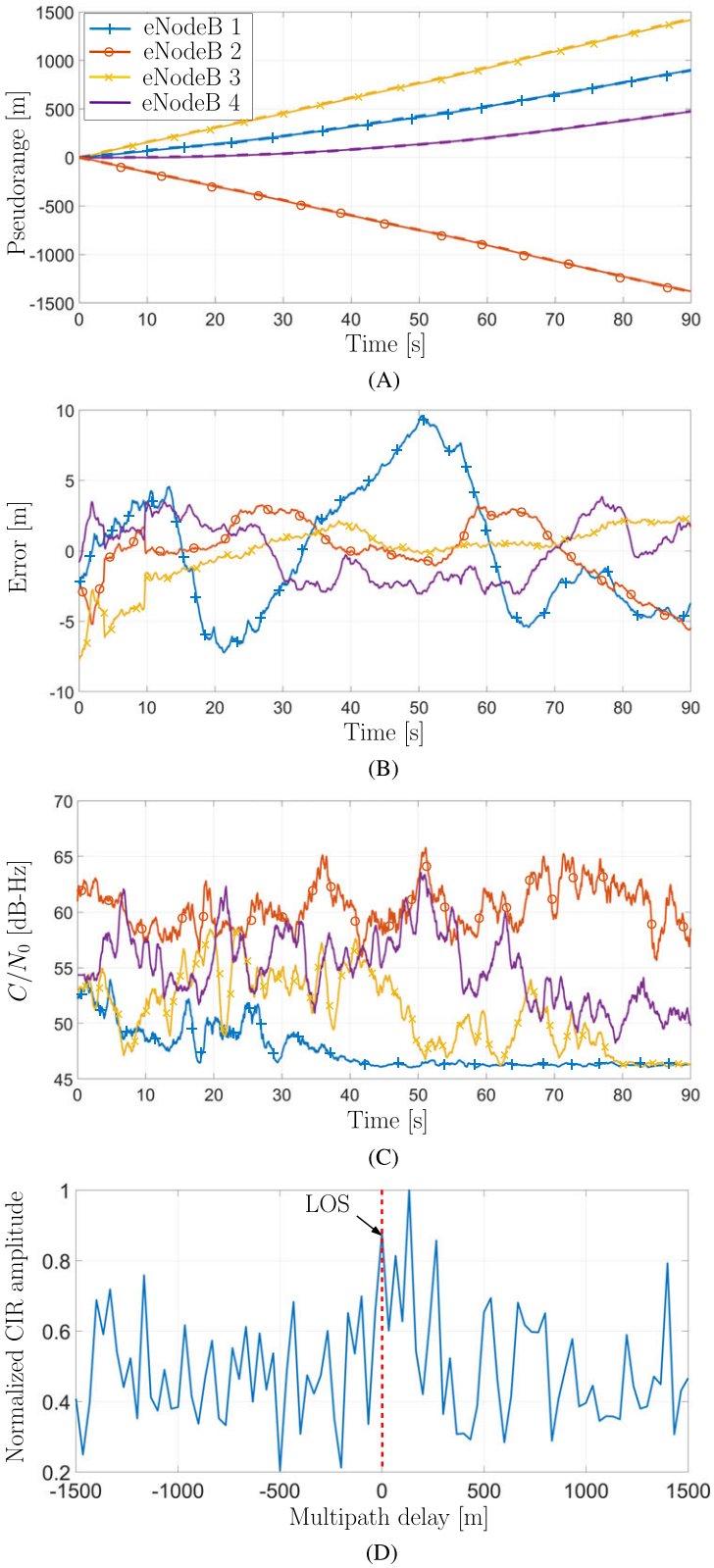

FIGURE 14 A, Measured pseudoranges and actual ranges for each eNodeB, plotted with dashed and solid lines, respectively. The initial values were removed for comparison purposes. B, The obtained error between the pseudoranges and the actual ranges, after removing the mean of the error. C, Measured C/N_0 of the received signal from each eNodeB. D, The normalized channel impulse response (CIR) of the received long-term evolution (LTE) signal from eNodeB 1 at time instant 40 s [Color figure can be viewed at wileyonlinelibrary.com and www.ion.org]

The clock error dynamics modeled in (22) are only valid for a GPSDO over short periods of time. When the measurement rate is significantly higher than the GPSDO correction rate, it can be assumed that the clock follows the model presented in Section 5 between each GPSDO correction. In this paper, the measurements are obtained every 10 milliseconds, while the GPSDO correction is performed usually less than once per second. Therefore, using the model in (22) is practical. The eNodeBs' clocks were modeled as OCXOs with $\{h_{0_s}\}_{i=1}^{N} = 2.6\times10^{-22}$ and $\{h_{-2_s}\}_{i=1}^{N} = 4\times10^{-26}$, while the receiver's clock was modeled as a TCXO with $h_{0_r} = 9.4\times10^{-20}$ and $h_{-2_r} = 3.8\times10^{-21}$. The process noise power spectral densities $\tilde{q}_x$ and $\tilde{q}_y$ were set to 0.1 (m^2/s^3), and the measurement noise standard deviation was set to 10 m^2, which were obtained empirically.

After collecting the LTE and GPS samples along the vehicle's trajectory, the stored LTE signals were processed using the proposed LTE receiver to obtain the pseudoranges. The GPS signal was processed using the generalized radionavigation interfusion (GRID) SDR.[57]

The DLL bandwidth was tuned between 0.05 and 0.2 Hz, and the PLL bandwidth was tuned between 4 and 8 Hz. In order to choose the loop bandwidth, it is required to balance the performance in the presence of noise against the performance for a moving receiver. Low loop bandwidth improves the performance in the presence of noise by increasing the averaging time. However, a longer averaging time degrades the performance of a moving receiver. Experimental results revealed that the PLL with high loop bandwidth would fail to track signals with low C/N_0. Therefore, the PLL bandwidth has to be decreased for low C/N_0. To capture the dynamics of a moving receiver, the DLL loop bandwidth, on the other hand, must be increased. Typically, with high C/N_0, the PLL bandwidth can be increased and lower bandwidth for the DLL can be chosen.

The ESPRIT design parameter was set to $P = 0.5M$. The integration was performed over four consecutive OFDM symbols carrying CRS in four slots. The characteristics of the eNodeBs to which the receiver was listening during the experiment are presented in Table 2. The GPS navigation solution was produced from 10 GPS satellites.

6.2 | Experimental results

Over the course of the experiment, the ground vehicle traversed a trajectory of 1.44 km in 90 seconds with an average speed of 16 m/s. In order to evaluate the channel condition, the ESPRIT algorithm was used to estimate the CIR at each frame of the received LTE signal over the course of the experiment. Figure 13 shows the probability of the relative (with respect to the first estimated path)

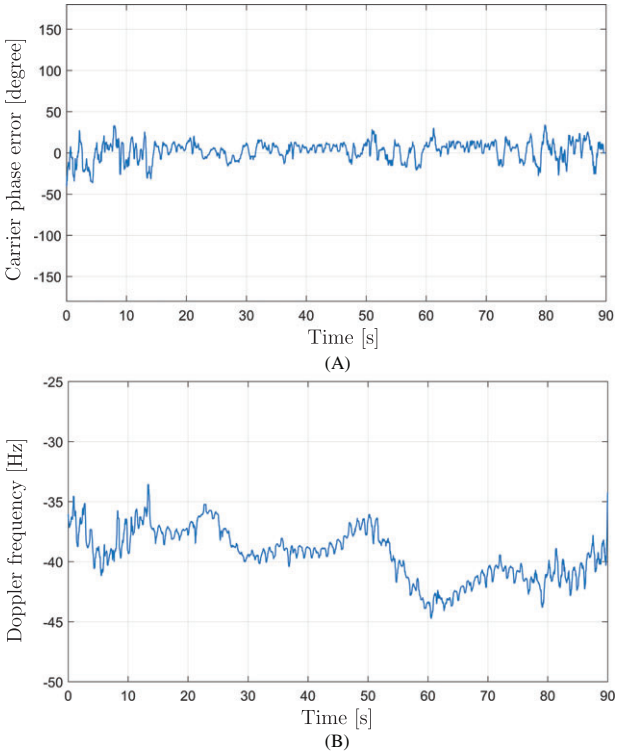

FIGURE 15 Tracking results for eNodeB 3: A, carrier phase error and B, Doppler frequency (Hz) [Color figure can be viewed at wileyonlinelibrary.com and www.ion.org]

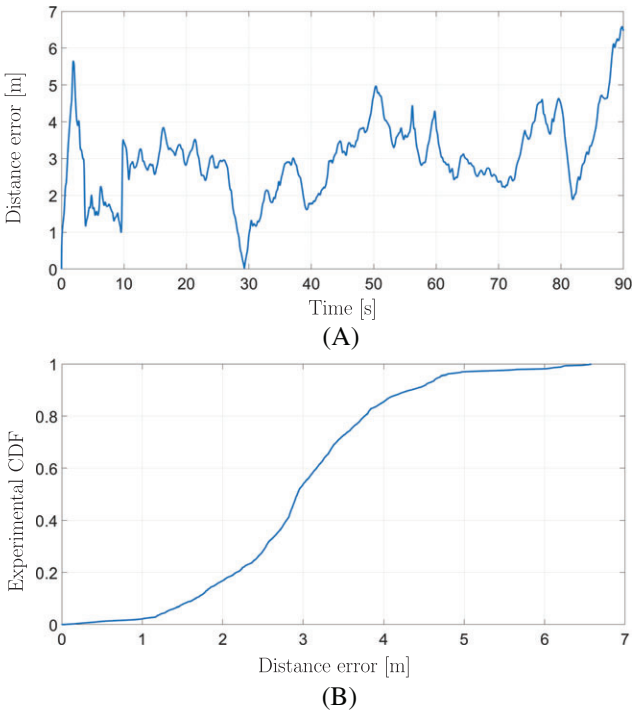

FIGURE 16 A, Distance error between the navigation solution obtained by the long-term evolution (LTE) software-defined receiver (SDR) and the GPS navigation solution over time. B, The cumulative distribution function (CDF) of the error [Color figure can be viewed at wileyonlinelibrary.com and www.ion.org]

attenuation and delay components of multipath for each eNodeB. The results showed that the average of the channel length L over the course of the experiment for eNodeBs 1 through 4 was 1.09, 4.29, 1.45, and 1.17, respectively, implying relatively less multipath compared with the extended typical urban (ETU) channel model with channel length of 9. In some environments, the received signal may be completely blocked resulting in an NLOS signal. Differentiating the LOS signal from the NLOS signal is outside the scope of this paper, and the received signal with the lowest TOA is assumed to be the LOS signal.

The obtained pseudoranges with the proposed LTE SDR for each eNodeB are shown in Figure 14A with dashed lines. The receiver had access to its actual position using the stored GPS signal. Therefore, the actual ranges of the receiver to each eNodeB were calculated and are shown in Figure 14A with solid lines. To enable comparison, the initial values of the pseudoranges and actual ranges are removed in Figure 14A. It can be seen that the change in pseudoranges follows the actual ranges closely.

Figure 14B shows the relative errors between the pseudoranges and their corresponding ranges. In this figure, it was assumed that the mean of each error is due to the difference of the clock biases between the receiver and the transmitter. Therefore, the mean of the obtained errors for each eNodeB was removed from the entire error, and the plotted errors have zero-mean. The results show that the standard deviation of the pseudorange errors for eNodeBs 1 through 4 is 4.55, 2.20, 1.96, and 2.04 m, respectively. The difference in the obtained standard deviations can be attributed to several factors, including (1) different transmission bandwidth, (2) different multipath environment, and (3) different clock drifts. Figure 14C shows the measured C/N_0 of the received signal from each eNodeB over the course of the experiment. It can be seen that eNodeB 1's C/N_0 drops to approximately 47 dB-Hz after 40 seconds. Figure 14D shows the CIR of the received signal from

TABLE 3 LTE navigation performance with proposed method

Performance Measure	Value, m
RMSE	3.17
Standard deviation	1.06
Maximum error	6.58

Abbreviations: LTE, long-term evolution; RMSE, root mean square error.

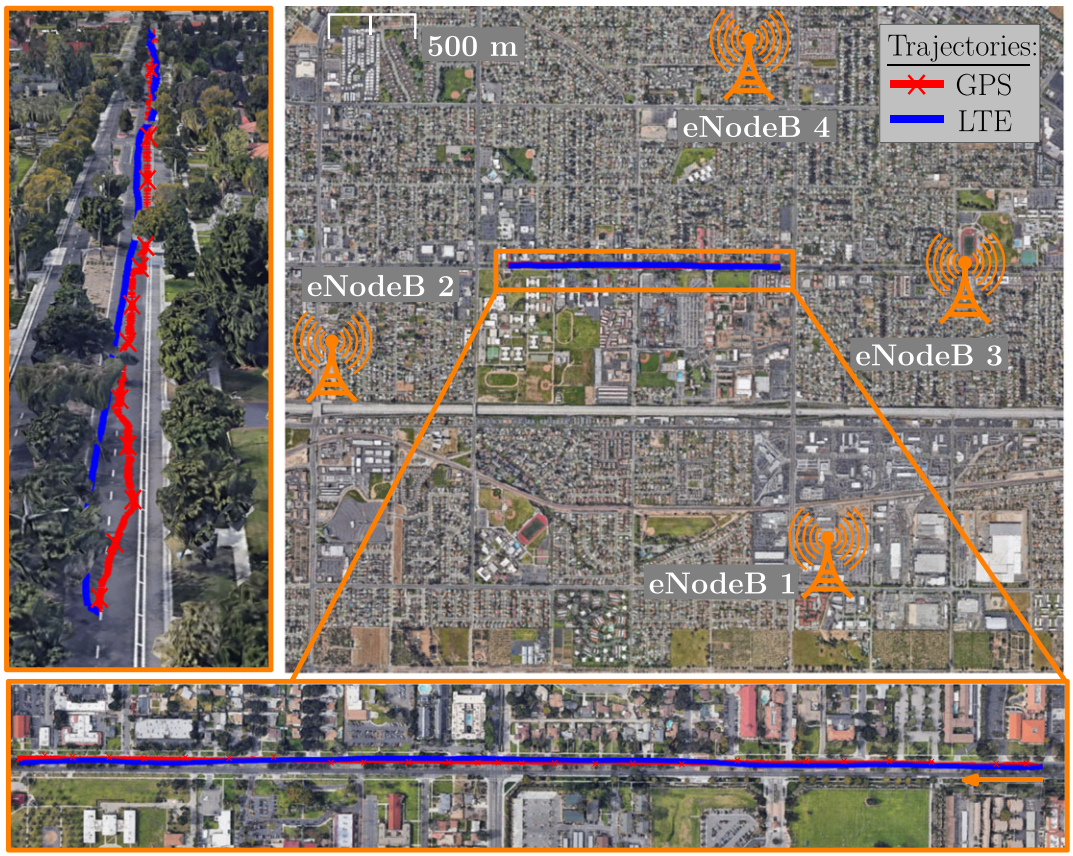

FIGURE 17 Environment layout, the eNodeBs' locations, and the traversed trajectory. The long-term evolution (LTE) navigation solution exhibited a root mean square error (RMSE) of 3.17 m, standard deviation of 1.06 m, and maximum error of 6.58 m from the GPS navigation solution over a trajectory of 1.44 km. Image: Google Earth [Color figure can be viewed at wileyonlinelibrary.com and www.ion.org]

eNodeB 1 at time instant 40 seconds. It can be seen that at this time instant, the noise level and multipath are significantly high resulting in low C/N_0. Although multipath is severe for this received signal and the C/N_0 is low, the estimated pseudorange obtained by the proposed receiver still follows the actual range closely. Figure 15A and 15B shows the tracking results for the carrier phase error and Doppler frequency, respectively, for eNodeB 3.

Figure 16A shows the distance error between the navigation solution obtained by the LTE SDR and that of the GPS navigation solution over time. The experimental cumulative distribution function (CDF) of the error is shown in Figure 16B. The environment layout, the eNodeBs' locations, and the entire trajectory are shown in Figure 17. Table 3 summarizes the LTE navigation performance.

6.3 | Comparison with other methods

A threshold-based receiver was tested in this environment in Shamaei et al.[30] With this receiver, signals from only three eNodeBs were trackable (ie, eNodeBs 2 through 4) and the resulting RMSE over the same traversed trajectory was 11.96 m, with standard deviation of 6.83 m, and a maximum error of 40.42 m. An earlier version of the receiver presented in this paper was tested in this environment as well.[35] The receiver used only a DLL and did not average over multiple LTE symbols, which is proposed in this paper. With the receiver in Shamaei et al,[35] signals from all four eNodeBs were trackable and the resulting RMSE over the same traversed trajectory was 5.36 m, with a standard deviation of 2.54 m, and a maximum error of 12.97 m. It can be seen that the receiver proposed in this paper produced a superior navigation performance. It is worth noting that GPS signals did not suffer from multipath as severely as the LTE signals, given that the sky was not obstructed above the receiver.

The performance of the proposed receiver is also compared with the ESPRIT and EKAT algorithms discussed in Driusso et al.[33] The ESPRIT algorithm is known to provide highly accurate TOA estimation. However, this method needs perfect knowledge of the CIR length L to provide accurate results. The MDL method is an approach that can be used to estimate L, but this method tends to overestimate the channel length. As a result, the ESPRIT TOA estimation has an outlier. The effect of this outlier can be reduced significantly using a Kalman filter and a predetermined threshold on the vehicle's speed, which is called EKAT in Driusso et al.[33] Figure 18 shows the pseudoranges obtained by the ESPRIT, EKAT, and the proposed receiver for all eNodeBs. It can be seen that the pseudoranges obtained by ESPRIT have significant outliers, which is improved in EKAT. The pseudoranges shown in Figure 18 are obtained using the same parameters as in Driusso et al.[33] It can be seen that the pseudoranges obtained by the proposed receiver are significantly more robust and accurate. For more explanation on the high error obtained using ESPRIT and EKAT algorithms, consider the results for eNodeB 1. As was discussed in Figure 14, the noise level and multipath effect for eNodeB 1 increase after 40

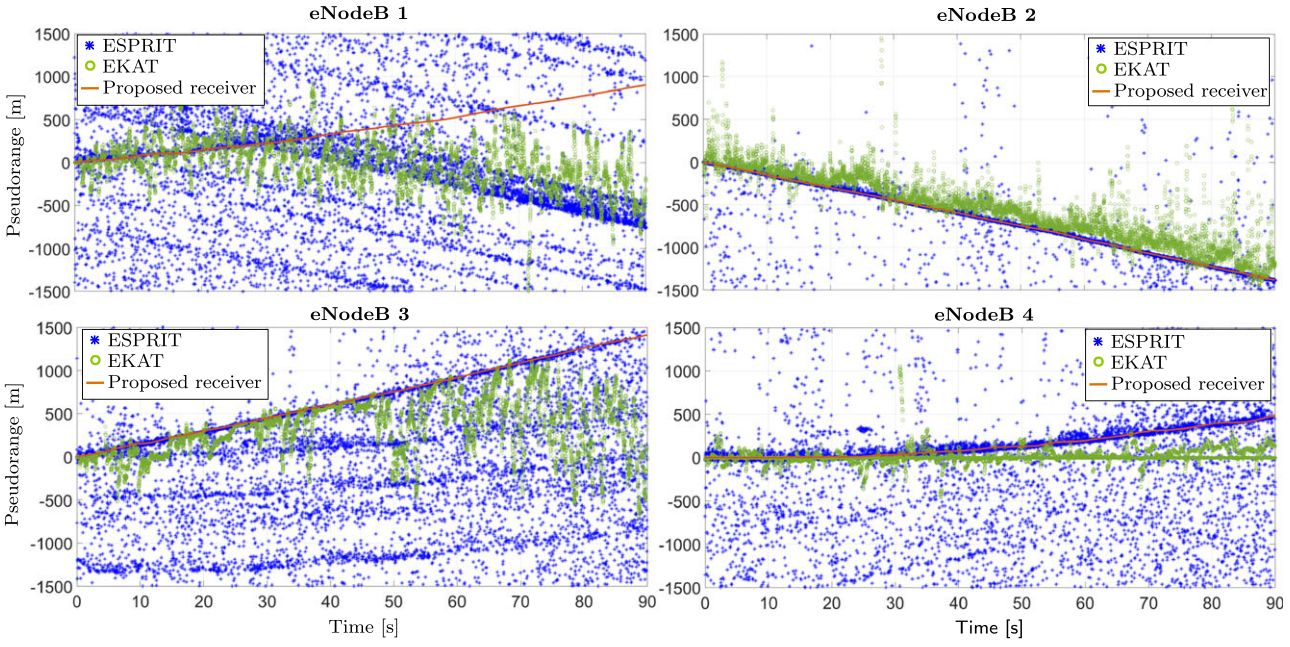

FIGURE 18 Estimated pseudoranges obtained by the proposed receiver, estimation of signal parameters by rotational invariance techniques (ESPRIT), and EKAT (ESPRIT and Kalman filter) algorithms for all the eNodeBs [Color figure can be viewed at wileyonlinelibrary.com and www.ion.org]

TABLE 4 Comparison of pseudorange errors obtained by each method

	ESPRIT		EKAT		Proposed Method	
	σ, [m]	Max Error, [m]	σ, [m]	Max Error, [m]	σ, [m]	Max Error, [m]
eNodeB 1	883.2	2102	495.6	1683	4.55	9.61
eNodeB 2	249.2	2981	176.6	2098	2.20	5.60
eNodeB 3	836.8	2431	422.1	1751	1.96	7.74
eNodeB 4	642.3	1884	148.4	1151	2.04	3.84

Abbreviations: EKAT, ESPRIT and Kalman filter; ESPRIT, estimation of signal parameters by rotational invariance techniques.

seconds. Under this condition, the MDL algorithm tends to overestimate the channel length and as a result, the noise components are detected as the signal components in the ESPRIT algorithm. Although the EKAT algorithm could remove some of the outliers in the estimated CIR by ESPRIT, it could not eliminate a continuous error in the CIR estimates obtained by the ESPRIT algorithm. Table 4 compares the pseudorange error statistics (standard deviation σ and maximum error) obtained with the proposed method versus the ESPRIT and EKAT algorithms.

In terms of complexity, the ESPRIT and EKAT algorithms have complexity on the order of $\mathcal{O}(N_c^3)$, which is mainly due to the SVD operator. However, the complexity of the proposed receiver is on the order of $\mathcal{O}(N_c \log N_c)$, which is due to the FFT operator. Since acquisition is performed either once before tracking starts or after tracking is lost, and since the majority of the processing time is spent in the tracking stage, when evaluating the complexity, only the tracking stage is considered.

7 | CONCLUSION AND FUTURE WORK

This paper presented a computationally efficient receiver design for navigating exclusively with LTE signals in multipath environments. The receiver mitigated multipath and produced an accurate navigation solution in an urban environment. A brief review of the LTE signal structure and the ranging signals was first discussed. The structure of the proposed receiver was presented. The statistics of the code phase error in a multipath and multipath-free environment were analyzed. The effect of time integration on the code phase error performance was evaluated. Experimental results comparing the navigation solutions obtained from GPS versus LTE utilizing the proposed receiver were provided. The experimental results showed an RMSE of 3.17 m, a standard deviation of 1.06 m, and a maximum error of 6.58 m over a 1.44 km trajectory. Finally, the proposed receiver's performance was compared against the ESPRIT and EKAT algorithms, demonstrating robust and accurate pseudoranges with a significantly lower computational cost.

In this paper, it was assumed that the power law model for the clock error dynamics is valid for a GPSDO where the measurement rate is significantly higher than the GPSDO correction rate. However, the usefulness of the power law model is in its application to the steady-state operation of the loop. The disciplining action can have the effect of significantly increasing the apparent white frequency noise since the control action is not an unconstrained random walk, but rather a result of a tight LPF and a slew-rate limiter. This, coupled with a discretized control action, can inject unusual features in the observed phase. Note that in practical applications, LTE eNodeBs are typically equipped with a GPSDO, while a receiver does not possess a GPSDO. Modeling the clock error dynamics for a GPSDO needs to be addressed in future work.

Characterization of the nonlinear behavior of the phase estimation for weak signal tracking and its resultant impact on the mean and variance models is one of the remaining challenges that needs to be addressed in future work.[58-60]

ACKNOWLEDGMENT

This work was supported in part by the Office of Naval Research (ONR) under grant N00014-16-1-2305. The authors would like to thank Joe Khalife for helpful discussions.

ORCID

Kimia Shamaei https://orcid.org/0000-0002-2930-7837
Zaher M. Kassas https://orcid.org/0000-0002-4388-6142

REFERENCES

1. Ji S, Chen W, Ding X, Chen Y, Zhao C, Hu C. Potential benefits of GPS/GLONASS/GALILEO integration in an urban canyon—Hong Kong. *J Navig*. 2010 October;63(4):681-693.
2. Saab S, Kassas Z. Map-based land vehicle navigation system with DGPS. *Proceedings of IEEE Intelligent Vehicle Symposium*, Vol. 1; 2002; Versailles, France. 209-214.
3. Saab S, Kassas Z. Power matching approach for GPS coverage extension. *IEEE Trans Intell Transp Syst*. 2006 June,7(2):156-166.
4. Wang L, Groves P, Ziebart Z. GNSS shadow matching: improving urban positioning accuracy using a 3D city model with optimized visibility scoring scheme. *NAVIGATION*. Fall 2013;60(3):195-207.
5. Yozevitch R, Moshe B. A robust shadow matching algorithm for GNSS positioning. *NAVIGATION*. Summer 2015;62(2):95-109.

6. Tsakiri M, Kealy A, Stewart M. Urban canyon vehicle navigation with integrated GPS/GLONASS/DR systems. *NAVIGATION*. Fall 1999;46(3):161-174.
7. Toledo-Moreo R, Betaille D, Peyret F. Lane-level integrity provision for navigation and map matching with GNSS, dead reckoning, and enhanced maps. *IEEE Trans Intell Transp Syst*. March 2010;11(1):100-112.
8. Kozak K, Alban M. Ranger: a ground-facing camera-based localization system for ground vehicles. *Proceedings of IEEE/ION (PLANS)*; April 2016; Savannah, GA, USA:170-178.
9. McEllroy J. *Navigation using signals of opportunity in the AM transmission band. Master's Thesis*. Ohio, USA: Air Force Institute of Technology, Wright-Patterson Air Force Base; 2006.
10. Fang S, Chen J, Huang H, Lin T. Is FM a RF-based positioning solution in a metropolitan-scale environment? A probabilistic approach with radio measurements analysis. *IEEE Trans Broadcast*. September 2009;55(3):577-588.
11. Thevenon P, Damien S, Julien O, et al. Positioning using mobile TV based on the DVB-SH standard. *NAVIGATION*. Summer 2011;58(2):71-90.
12. Pesyna K, Kassas Z, Humphreys T. Constructing a continuous phase time history from TDMA signals for opportunistic navigation. *Proceedings of IEEE/ION PLANS*; April 2012; Myrtle Beach, SC, USA:1209-1220.
13. Kassas Z. Collaborative opportunistic navigation. *IEEE Aerosp Electron Syst Mag*. 2013;28(6):38-41.
14. Kassas Z. *Analysis and synthesis of collaborative opportunistic navigation systems. Ph.D. dissertation*: The University of Texas at Austin; 2014.
15. Faragher R, Harle R. Towards an efficient, intelligent, opportunistic smartphone indoor positioning system. *NAVIGATION*. Spring 2015;62(1):55-72.
16. Kassas Z, Morales J, Shamaei K, Khalife J. LTE steers UAV. *GPS World Mag*. April 2017;28(4):18-25.
17. Kassas Z, Khalife J, Shamaei K, Morales J. I hear, therefore I know where I am: compensating for GNSS limitations with cellular signals. *IEEE Signal Process Mag*. September 2017;34:111-124.
18. Yang C, Nguyen T, Blasch E. Mobile positioning via fusion of mixed signals of opportunity. *IEEE Aerosp Electron Syst Mag*. April 2014;29(4):34-46.
19. Khalife J, Shamaei K, Kassas Z. A software-defined receiver architecture for cellular CDMA-based navigation. *Proceedings of IEEE/ION PLANS*; April 2016; Savannah, GA, USA: 816-826.
20. Morales J, Roysdon P, Kassas Z. Signals of opportunity aided inertial navigation. *Proceedings of 29th International Technical Meeting of the Satellite Division of The Institute of Navigaiton (ION GNSS+2016)*; September 2016; Portland, OR, USA: 1492-1501.
21. Morales J, Khalife J, Kassas Z. GNSS vertical dilution of precision reduction using terrestrial signals of opportunity. Proceedings of the 2016 International *Technical Meeting of The Institute of Navigation*; January 2016; Monterey, CA, USA: 664-669.
22. Morales J, Khalife J, Kassas Z. Opportunity for accuracy. *GPS World Mag*. March 2016;27(3):22-29.
23. Shamaei K, Khalife J, Kassas Z. Comparative results for positioning with secondary synchronization signal versus cell specific reference signal in LTE systems. *Proceedings of the 2017 International Technical Meeting of the Institute of Navigation*; January 2017; Monterey, CA, USA: 1256-1268.
24. del Peral-Rosado J, Lopez-Salcedo J, Seco-Granados G, Zanier F, Crisci M. Preliminary analysis of the positioning capabilities of the positioning reference signals of 3GPP LTE. *Proceedings of European Workshop on GNSS Signals and Signal Processing*. Toulouse, France; 2011.
25. del Peral-Rosado J, Lopez-Salcedo J, Seco-Granados G, Zanier F, Crisci M. Achievable localization accuracy of the positioning reference signal of 3GPP LTE. *Proceedings of the International Conference on Localization and GNSS*; 2012; Starnberg, Germany: 1-6.
26. del Peral-Rosado J, Lopez-Salcedo J, Seco-Granados G, Zanier F, Crisci M. Evaluation of the LTE positioning capabilities under typical multipath channels. *Proceedings of Advanced Satellite Multimedia Systems Conference and Signal Processing for Space Communications Workshop*; 2012; Baiona, Spain:139-146.
27. Shamaei K, Khalife J, Kassas Z. Ranging precision analysis of LTE signals. *Proceedings of European Signal Processing Conference*; 2017; Kos, Greece: 2788-2792.
28. del Peral-Rosado J, Lopez-Salcedo J, Seco-Granados G, et al. Software-defined radio LTE positioning receiver towards future hybrid localization systems. *Proceedings of International Communication Satellite Systems Conference*. Florence, Italy; 2013: 14-17.
29. del Peral-Rosado J, Parro-Jimenez J, Lopez-Salcedo J, et al. Comparative results analysis on positioning with real LTE signals and low-cost hardware platforms. *Proceedings of Satellite Navigation Technologies and European Workshop on GNSS Signals and Signal Processing*; 2014; Noordwijk, Netherlands: 1-8.a.
30. Shamaei K, Khalife J, Kassas Z. Performance characterization of positioning in LTE systems. *Proceedings of the 29th International Technical Meeting of the Satellite Division of The Institute of Navigation (ION GNSS+2016)*; 2016; Portland, OR, USA: 2262-2270.
31. Knutti F, Sabathy M, Driusso M, Mathis H, Marshall C. Positioning using LTE signals. *Proceedings of Navigation Conference in Europe*. Bordeaux, France; 2015:1-8.
32. Pittino F, Driusso M, Torre A, Marshall C. Outdoor and indoor experiments with localization using LTE signals. *Proceedings European Navigation Conference*; May 2017; Lausanne, Switzerland:311-321.
33. Driusso M, Babich F, Knutti F, Sabathy M, Marshall C. Estimation and tracking of LTE signals time of arrival in a mobile multipath environment. *Proceedings of International Symposium on Image and Signal Processing and Analysis*; September 2015; Zagreb, Croatia: 276-281.
34. Driusso M, Marshall C, Sabathy M, Knutti F, Mathis H, Babich F. Vehicular position tracking using LTE signals. *IEEE Trans Veh Technol*. April 2017;66(4):3376-3391.
35. Shamaei K, Khalife J, Bhattacharya S, Kassas Z. Computationally efficient receiver design for mitigating multipath for positioning with LTE signals. *Proceedings of 30th International Technical Meeting of the Satellite Division of The Institute of Navigation (ION GNSS+2017)*; 2017; Portland, OR:3751-3760.
36. Roy R, Kailath T. ESPRIT—estimation of signal parameters via rotational invariance techniques. *IEEE Trans Acoust Speech Signal Process*. July 1989;37(7):984-995.
37. 3GPP. Evolved universal terrestrial radio access (E-UTRA); physical channels and modulation, *3rd Generation Partnership Project (3GPP)*, TS 36211. Available at: http://www.3gpp.org/ftp/Specs/html-info/36211.htm; January 2011.
38. Sesia S, Toufik I, Baker M. *LTE—The UMTS Long Term Evolution: From Theory to Practice*. New Jersey: Wiley Publishing; 2009.
39. Shamaei K, Khalife J, Kassas Z. Pseudorange and multipath analysis of positioning with LTE secondary synchronization signals. *Proceedings of Wireless Communications and Networking Conference*; 2018; Barcelona, Spain: 286-291.

40. van de Beek J, Sandell M, Borjesson P. ML estimation of time and frequency offset in OFDM systems. *IEEE Trans Signal Process*. July 1997;45(7):1800-1805.
41. Fischer S. Observed time difference of arrival (OTDOA) positioning in 3GPP LTE. Technical Report, San Diego, California, Qualcomm Technologies, Inc.; 2014.
42. Hofer M, McEachen J, Tummala M. Vulnerability analysis of LTE location services. *Proceedings of Hawaii International Conference on System Sciences*; January 2014; Waikoloa, HI, USA:5162-5166.
43. Ulmschneider M, Gentner C. Multipath assisted positioning for pedestrians using LTE signals. *Proceedings of IEEE/ION PLANS*; April 2016; Savannah, GA, USA:386-392.
44. Speth M, Fechtel S, Fock G, Meyr H. Optimum receiver design for wireless broad-band systems using OFDM: part I. *IEEE Trans Commun*. November 1999;47(11):1668-1677.
45. Yang B, Letaief K, Cheng R, Cao Z. Timing recovery for OFDM transmission. *IEEE J Sel Areas Commun*. November 2000;18(11):2278-2291.
46. Yang B, Letaief K, Cheng R, Cao Z. Channel estimation for OFDM transmission in multipath fading channels based on parametric channel modeling. *IEEE Trans Commun*. 2001;49(3):467-479.
47. Wax M, Kailath T. Detection of signals by information theoretic criteria. *IEEE Trans Acoust Speech Signal Process*. April 1985;33(2):387-392.
48. Speth M, Fechtel S, Fock G, Meyr H. Optimum receiver design for OFDM-based broadband transmission—part II: a case study. *IEEE Trans Commun*. April 2001;49(4):571-578.
49. Misra P, Enge P. *Global Positioning System: Signals, Measurements, and Performance*. Second. Lincoln, MA: Ganga-Jamuna Press; 2010.
50. Kaplan E, Hegarty C. *Understanding GPS: Principles and Applications*. Second. Norwood, MA, USA: Artech House; 2005.
51. Wesson KD, Pesyna KM, Bhatti JA, Humphreys TE. Opportunistic frequency stability transfer for extending the coherence time of GNSS receiver clocks. *Proceedings of the 23rd International Technical Meeting of the Satellite Division of the Institute of Navigation (ION GNSS2010)*; September 2010; Portland, OR, USA:2959-2968.
52. Bar-Shalom Y, Li X, Kirubarajan T. *Estimation with Applications to Tracking and Navigation*. New York, NY: John Wiley; 2002.
53. Kassas Z, Ghadiok V, Humphreys T. Adaptive estimation of signals of opportunity. *Proceedings of 27th International Technical Meeting of the Satellite Division of The Institute of Navigation (ION GNSS+2014)*; September 2014; Tampa, FL, USA:1679-1689.
54. Morales J, Kassas Z. Optimal collaborative mapping of terrestrial transmitters: receiver placement and performance characterization. *IEEE Trans Aerosp Electron Syst*. April 2018;54(2):992-1007.
55. Bladsjo D, Hogan M, Ruffini S. Synchronization aspects in LTE small cells. *IEEE Commun Mag*. September 2013;51(9):70-77.
56. Mancini O. Tutorial: precision frequency generation utilizing OCXO and rubidium atomic standards with applications for commercial, space, military, and challenging environments. Technical Report, New York, *IEEE*, Long Island Chapter.
57. Humphreys T, Bhatti J, Pany T, Ledvina B, O'Hanlon B. Exploiting multicore technology in software-defined GNSS receivers. *Proceedings of 22nd International Technical Meeting of the Satellite Division of The Institute of Navigation (ION GNSS 2009)*; 2009; Savannah, GA, USA:326-338.
58. Ward W. Performance comparisons between FLL, PLL and a novel FLL-assisted-PLL carrier tracking loop under RF interference conditions. *Proceedings of the 11th International Technical Meeting of the Satellite Division of The Institute of Navigation (ION GPS 1998)*; 1998; Nashville, TN, USA:783-195.
59. Betz J, Kolodziejski K. Extended theory of early-late code tracking for a bandlimited GPS receiver. *NAVIGATION*. Fall 2000;43(3):211-226.
60. Betz J. Design and performance of code tracking for the GPS M code signal. *Proceedings of the 13th International Technical Meeting of the Satellite Division of the Institute of Navigation (ION GPS 2000)*; September 2000; Salt Lake City, UT, USA: 2140-2150.

How to cite this article: Shamaei K, Kassas ZM. LTE receiver design and multipath analysis for navigation in urban environments. *NAVIGATION*. 2018;65:655–675. https://doi.org/10.1002/navi.272